

University of Windsor

Scholarship at UWindor

Electronic Theses and Dissertations

Theses, Dissertations, and Major Papers

2008

Investigation of an Atomic Force Microscope (AFM) probe under electrostatic actuation

Liton Ghosh
University of Windsor

Follow this and additional works at: <https://scholar.uwindsor.ca/etd>

Recommended Citation

Ghosh, Liton, "Investigation of an Atomic Force Microscope (AFM) probe under electrostatic actuation" (2008). *Electronic Theses and Dissertations*. 7884.
<https://scholar.uwindsor.ca/etd/7884>

This online database contains the full-text of PhD dissertations and Masters' theses of University of Windsor students from 1954 forward. These documents are made available for personal study and research purposes only, in accordance with the Canadian Copyright Act and the Creative Commons license—CC BY-NC-ND (Attribution, Non-Commercial, No Derivative Works). Under this license, works must always be attributed to the copyright holder (original author), cannot be used for any commercial purposes, and may not be altered. Any other use would require the permission of the copyright holder. Students may inquire about withdrawing their dissertation and/or thesis from this database. For additional inquiries, please contact the repository administrator via email (scholarship@uwindsor.ca) or by telephone at 519-253-3000ext. 3208.

**Investigation of an
Atomic Force Microscope (AFM)
Probe under Electrostatic Actuation**

by
Liton Ghosh

A Thesis
Submitted to the Faculty of Graduate Studies
through Electrical Engineering
in Partial Fulfillment of the Requirements for
the Degree of Master of Applied Science at the
University of Windsor

Windsor, Ontario, Canada

2008

© Liton Ghosh



Library and
Archives Canada

Bibliothèque et
Archives Canada

Published Heritage
Branch

Direction du
Patrimoine de l'édition

395 Wellington Street
Ottawa ON K1A 0N4
Canada

395, rue Wellington
Ottawa ON K1A 0N4
Canada

Your file *Votre référence*

ISBN: 978-0-494-47087-9

Our file *Notre référence*

ISBN: 978-0-494-47087-9

NOTICE:

The author has granted a non-exclusive license allowing Library and Archives Canada to reproduce, publish, archive, preserve, conserve, communicate to the public by telecommunication or on the Internet, loan, distribute and sell theses worldwide, for commercial or non-commercial purposes, in microform, paper, electronic and/or any other formats.

The author retains copyright ownership and moral rights in this thesis. Neither the thesis nor substantial extracts from it may be printed or otherwise reproduced without the author's permission.

AVIS:

L'auteur a accordé une licence non exclusive permettant à la Bibliothèque et Archives Canada de reproduire, publier, archiver, sauvegarder, conserver, transmettre au public par télécommunication ou par l'Internet, prêter, distribuer et vendre des thèses partout dans le monde, à des fins commerciales ou autres, sur support microforme, papier, électronique et/ou autres formats.

L'auteur conserve la propriété du droit d'auteur et des droits moraux qui protègent cette thèse. Ni la thèse ni des extraits substantiels de celle-ci ne doivent être imprimés ou autrement reproduits sans son autorisation.

In compliance with the Canadian Privacy Act some supporting forms may have been removed from this thesis.

Conformément à la loi canadienne sur la protection de la vie privée, quelques formulaires secondaires ont été enlevés de cette thèse.

While these forms may be included in the document page count, their removal does not represent any loss of content from the thesis.

Bien que ces formulaires aient inclus dans la pagination, il n'y aura aucun contenu manquant.



Canada

AUTHOR'S DECLARATION OF ORIGINALITY

I hereby certify that I am the sole author of this thesis and that no part of this thesis has been published or submitted for publication.

I certify that, to the best of my knowledge, my thesis does not infringe upon anyone's copyright nor violate any proprietary rights and that any ideas, techniques, quotations, or any other material from the work of other people included in my thesis, published or otherwise, are fully acknowledged in accordance with the standard referencing practices. Furthermore, to the extent that I have included copyrighted material that surpasses the bounds of fair dealing within the meaning of the Canada Copyright Act, I certify that I have obtained a written permission from the copyright owner(s) to include such material(s) in my thesis and have included copies of such copyright clearances to my appendix.

I declare that this is a true copy of my thesis, including any final revisions, as approved by my thesis committee and the Graduate Studies office, and that this thesis has not been submitted for a higher degree to any other University or Institution.

ABSTRACT

This thesis develops a readily computable closed-form analytical model to determine the pull-in voltage of an Atomic Force Microscope (AFM) probe under electrostatic actuation. The analytical model has been derived based on the Euler-Bernoulli beam theory, Taylor series expansion of the electrostatic energy stored in the AFM probe, and deflection function of the first natural mode of a cantilever beam. The model takes account of the electrostatic energy associated with the fringing field capacitances between the AFM probe cantilever and the substrate to develop a more accurate model of the stored electrostatic energy after the system is biased with a DC voltage. The developed energy model is then used to develop a highly accurate closed-form model for the pull-in voltage of the AFM probe. The developed closed-form model has been verified by comparing the model predicted values with published experimental results with a maximum deviation of 3.36%. The model has also been compared with a published curve model and 3-D electromechanical finite element analysis (FEA) results. The results are found to be in excellent agreement.

To My Parents

ACKNOWLEDGEMENTS

I want to take the opportunity to acknowledge the people without whom this work would not have been possible. Firstly I want to express my sincere gratitude to my thesis supervisor, Dr. Sazzadur Chowdhury, for giving me the opportunity to work in the field of MEMS and Atomic Force Microscope, for his expert guidance and financial support, as well as for accepting topic of my thesis.

I would like to thank the Natural Sciences and Engineering Research Council of Canada (NSERC) and Ontario Centers of Excellence for supporting my research. I would like to thank the additional generous support provided by the Canadian Microelectronics Corporation (CMC), and the IntelliSense Software Corporation of Woburn, MA. I want to extend a very special thank to John Bloomsburgh of IntelliSense Software Corporation for helping me in carrying out the finite element analysis.

Thanks to Dr. Roberto Muscedere for arranging me a high performance machine in Research Center for Integrated Microsystems (RCIM) lab for running simulations for my project and also for the helps he did to me whenever I had any problem with those machines.

I would like to express my deepest gratitude to friends and co-workers who shaped the warm environment at University of Windsor. Special thanks to Jose Martinez-Quijada for helping me out with IntelliSuite and for his brother like motivation. I would like to give a big thank to my friend, Peng Chang's for his moral supports and inspirations.

The greatest acknowledgement to my mother, Tulshi Ghosh, to my father, Bimal Ghosh and to my brother, Dipon Ghosh, whose love has accompanied me far away from Bangladesh, from where their efforts brought reality to my dream of completing the degree of Master of Applied Science in Canada, giving me unconditional and generous support that allowed me to live without lacking anything. A special thanks to my mother for bringing me up right and for making me what I am.

Finally, I would like to thank my friends in Bangladesh whose inspiration and motivation encouraged me a lot for last two years in Canada.

TABLE OF CONTENTS

AUTHOR'S DECLARATION OF ORIGINALITY	iii
ABSTRACT	iv
DEDICATION.....	v
ACKNOWLEDGEMENTS	vi
LIST OF TABLES	xi
LIST OF FIGURES	xii
LIST OF APPENDICES	xiv
CHAPTER 1: INTRODUCTION.....	1
1.1 Goals.....	1
1.2 Background	2
1.2.1 Atomic Force Microscope Fundamentals	2
1.2.2 State of the Art in Pull-in Voltage modeling of an AFM Probe.....	6
1.2.3 Limitations of Existing Models.....	9
1.3 Scientific Approach to Solve the Problem	10
1.4 Principal Results	10
1.5 Organization of Thesis.....	11
CHAPTER 2: DEVICE MODELING CONSIDERATIONS.....	13
2.1 Geometry of an Atomic Force Microscope probe.....	13
2.2 Energy of AFM Probe-Substrate System	15
2.2.1 Mechanical Bending Energy	16

2.2.2	Electrostatic Energy.....	16
2.2.3	Van der Waals Energy.....	17
CHAPTER 3: ELECTROSTATIC ENERGY MODELING		19
3.1	Capacitance Associated with AFM Probe cantilever	19
3.2	Capacitance Associated with AFM Tip Cone.....	23
3.3	Capacitance Associated with AFM Tip Apex.....	23
3.4	Electrostatic Energy of AFM Probe-Substrate System.....	24
CHAPTER 4: PULL-IN VOLTAGE MODELING.....		25
4.1	Total Energy of AFM Probe-Substrate System	25
4.2	Pull-in Voltage Closed-Form Model.....	29
CHAPTER 5: FEA MODELING		35
5.1	Construction of Atomic Force Microscope Probes	35
5.1.1	Geometry of First Probe.....	36
5.1.2	Geometry of Second Probe.....	39
5.2	Meshing of Atomic Force Microscope Probes.....	42
5.2.1	Meshing of the Probes	44
CHAPTER 6: MODEL VERIFICATION.....		50
6.1	Comparison with Experimentally Determined Values and Values Determined from a Published Model	50
6.2	Comparison with Finite Element Analysis (FEA) Results	54
CONCLUSION		63
REFERENCES.....		66
APPENDIX A		70

APPENDIX B..... 80

VITA AUCTORIS 82

LIST OF TABLES

Table 1. Specifications of AFM probes	36
Table 2. AFM probe Material properties (AFM probe 1).....	51
Table 3. Pull-in Voltage Comparison for Different Methods (AFM probe 1).....	51
Table 4. Pull-in Voltage comparison (AFM probe 1).....	52
Table 5. Pull-in Voltage from FEA (AFM probe 1)	59
Table 6. Pull-in Voltage from FEA (AFM probe 2)	59
Table 7. Pull-in Voltage Comparison with FEA and New Model (AFM probe 1).....	60
Table 8. Pull-in Voltage Comparison with FEA and New Model (AFM probe 2).....	60

LIST OF FIGURES

Figure 1. Block Diagram of Atomic Force Microscope System.....	3
Figure 2. Close up Views of Atomic Force Microscope probe. (a-d) SEM images of an AFM probe (Courtesy: Nanosensors) and (e-f) different parts of AFM probe.....	5
Figure 3. Microfabricated cantilever beam [13]. (a) Before pull-in, (b) After pull-in.....	6
Figure 4. A curled beam [14].....	6
Figure 5. A schematic diagram of the AFM probe model used in [12] showing parameter notations.....	7
Figure 6. A schematic diagram of AFM probe-substrate system showing the cantilever length L , width w , thickness t and the height of the cone H	14
Figure 7. A line diagram of the AFM probe showing the radius R of the spherical apex of the cone, half opening angel θ of the cone, and the inclination angel β_{lever} of the cantilever with respect to substrate plane.	14
Figure 8. A schematic diagram of AFM probe-substrate system showing different forces acting on AFM probe.....	15
Figure 9. A schematic diagram of the AFM probe-substrate system showing various capacitance components.....	17
Figure 10. Schematic diagram of AFM probe cantilever arrangement.....	20
Figure 11. Geometry of AFM probe 1. (a) Front view of whole of the AFM probe-substrate system, (b) Side view of the AFM probe, (c) Orthogonal view of the AFM probe, (d) Side view of the pyramidal tip cone and the part of cantilever, (e) Spherical tip apex at the end of the tip.....	39
Figure 12. Geometry of AFM probe 2. (a) Front view of whole of the AFM probe-substrate system, (b) Side view of the AFM probe, (c) Orthogonal view of the AFM probe, (d) Side view of the pyramidal tip cone and the part of cantilever, (e) Spherical tip apex at the end of the tip.....	42
Figure 13. Different mesh sizes for different part of AFM probe 1. (a) Front view of the meshing of the AFM probe and the substrate, (b) Side view of the meshing of the pyramidal tip cone and the substrate, (c) Front view of the meshing of the tip apex, (d) Side view of the meshing of tip apex.....	46

Figure 14. Different mesh sizes for different part of AFM probe 2. (a) Front view of the meshing of the AFM probe and the substrate, (b) Side view of the meshing of the pyramidal tip cone and the substrate, (c) Front view of the meshing of the tip apex, (d) Side view of the meshing of tip apex.....	48
Figure 15. Pull-in voltage comparison of new closed-form model and published curve model in [12].....	53
Figure 16. Initial distance vs. Pull-in voltage curve redrawn from [12].....	54
Figure 17. Pull-in of the spherical tip apex of AFM probe 1 onto the substrate. (a) Front view (b) Side view.	55
Figure 18. Pull-in of the spherical tip apex of AFM probe 2 onto the substrate. (a) Front view (b) Side view.	56
Figure 19. Visualization of the displacement of different parts of AFM probe 1 in a color scale.....	57
Figure 20. Visualization of the displacement of different parts of AFM probe 2 in a color scale.....	58

LIST OF APPENDICES

APPENDIX A: MATLAB SCRIPTS	70
APPENDIX B: DEFINITION OF USED SYMBOLS	80

CHAPTER 1

INTRODUCTION

1.1 Goals

With the recent growth of the use of Atomic Force Microscopy (AFM) for surface characterization, nanoscale feature extraction, and nanoparticle manipulation, there is a need for a readily computable but accurate closed-form analytical model to determine the pull-in voltage of an AFM probe under electrostatic actuation. If the applied bias voltage is equal or greater than a certain limit called the pull-in voltage, the probe collapses on the substrate (surface under investigation) due to an electrostatic attraction force between the deformable probe and the fixed substrate. In order to avoid this pull-in problem, knowledge of load-deflection characteristic and accurate determination of the pull-in voltage is critical for proper operation of an AFM probe. The overall goal of this thesis is to develop, demonstrate and validate a readily computable closed-form model to determine the pull-in voltage of an AFM probe under electrostatic actuation.

Based on this objective, the specific goals of this research work have been set as follows:

1. Develop a highly accurate analytical model for the electrostatic energy in Atomic Force Microscope (AFM) probe-substrate system.
2. Use the developed energy model to develop a readily computable highly accurate closed-form analytical model for the pull-in voltage of an Atomic Force Microscope probe and provide load-deflection characteristic of an AFM probe subjected to electrostatic actuation.

3. Verify the accuracy of the developed closed-form pull-in voltage model by comparing the model predicted values with results from experimental, 3-D electromechanical Finite Element Analysis (FEA), and results from other published models.

1.2 Background

1.2.1 Atomic Force Microscope Fundamentals

Atomic Force Microscope was first invented by Binnig [1]. AFM is a type of Scanning Probe Microscope with sub-nanometer scale resolutions. Scanning Tunneling Microscope (STM) has the ability to resolve atomic structure of a sample but it can only be applied to conductive or semi-conductive specimens. To extend the technique to a wider variety of materials including insulators, AFM was developed in 1986. AFM operates under ambient or near ambient condition and can even be used in a liquid environment. AFM can be used on a wide variety of surface types, ranging from hard and crystalline to soft and pliable, even living entities like cell specimens.

Primarily AFM probe has been extensively used to image the surface of any sample. Later on it's use has been extended to obtain information about surface properties such as local surface potentials [2], surface charges [3-4], surface polarization forces [5], magnetic properties of surfaces [6]. However, in recent years, AFM has been identified as a powerful nanolithography tool [7-8] and some researchers demonstrated that AFM can be used to manipulate nanoparticles [9-12]. In [9-11] electrical manipulation of nanoparticles with AFM using AC voltages were demonstrated. In [12] DC voltage was used to manipulate chargeable particles in dry environment.

Figure 1 shows the basic components and working principles of an AFM system.

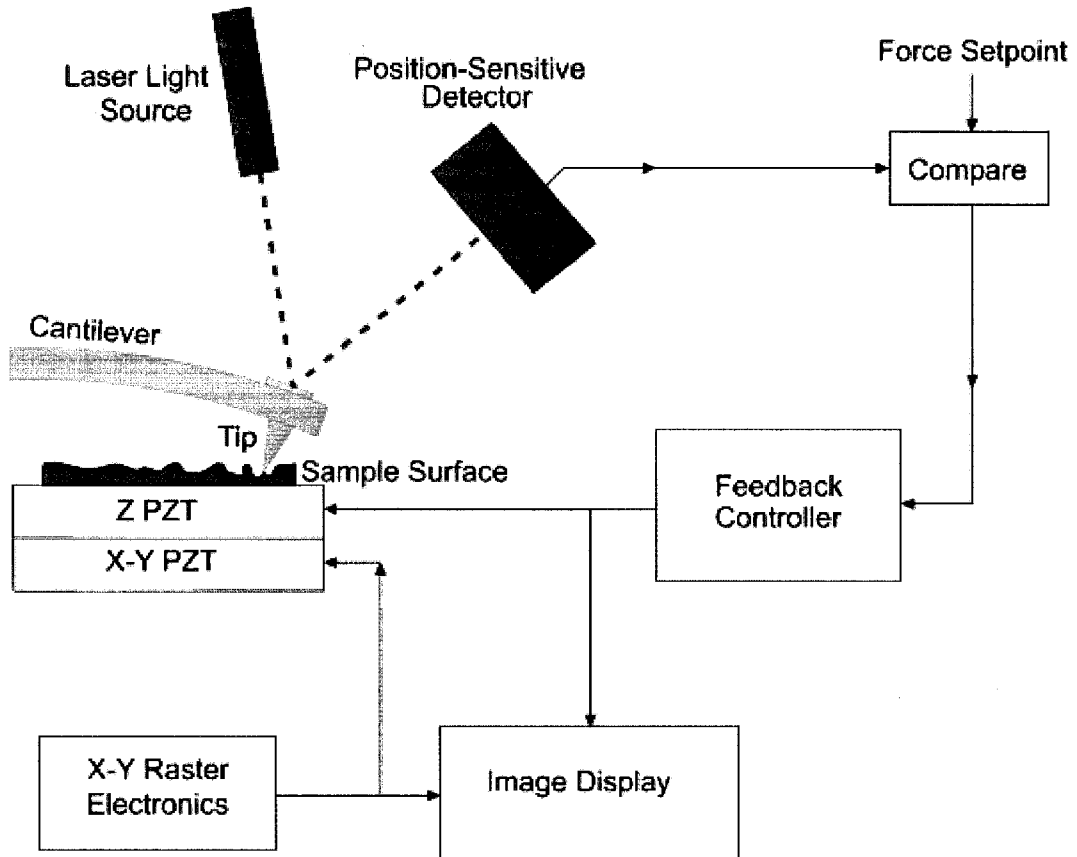


Figure 1. Block Diagram of Atomic Force Microscope System

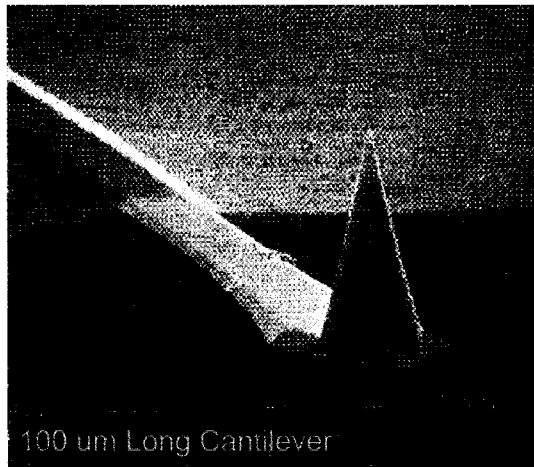
An Atomic Force Microscope is constructed using

- Piezoelectric Materials
- Feedback Control
- Force Sensors

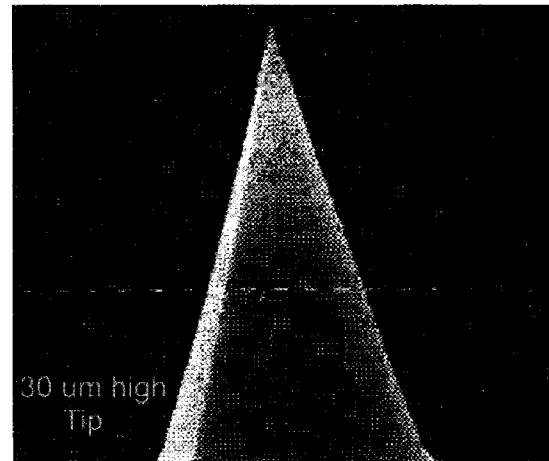
In the system, a microfabricated cantilever with a sharp tip at the end is used as a force sensor which is called the AFM probe. When the tip is brought closer to the surface, the forces between the tip and the sample cause the cantilever to bend. This motion is detected optically by the deflection of a laser beam (typically 635 nm Ar laser) which is reflected off the back of the cantilever. This detected signal is compared and then fed to feedback controller. The feedback controller keeps the force constant by controlling the expansion of the Z piezoelectric transducer. The X-Y piezoelectric ceramics are used to scan the probe across the surface in a raster-like pattern. By monitoring the voltage on the Z piezoelectric transducer, an image of the surface is obtained.

Figure 2 (a-d) shows Scanning Electron Microscope (SEM) images of a real AFM probe. Figure 2 (e-f) shows the conceptual line diagram of an AFM probe. An AFM probe can be divided into 3 parts.

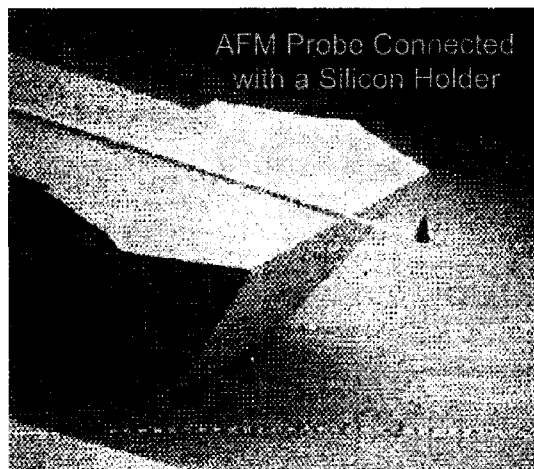
- Cantilever
- Tip Cone
- Spherical Tip Apex



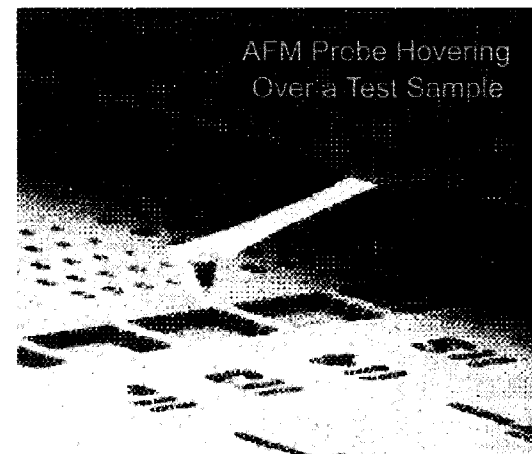
(a)



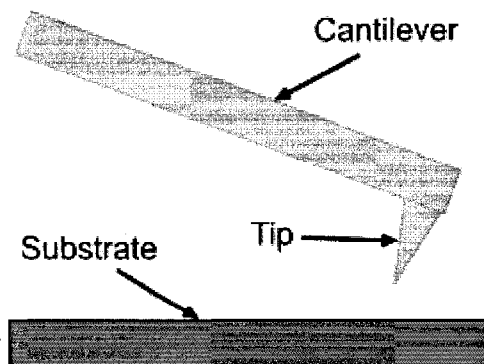
(b)



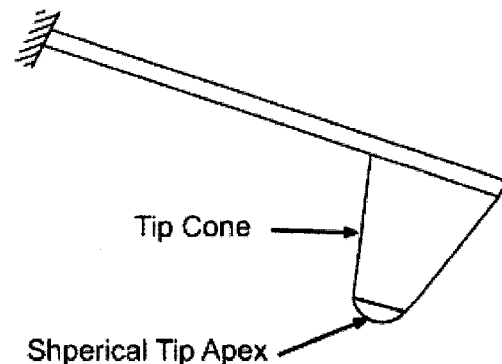
(c)



(d)



(e)



(f)

Figure 2. Close up Views of Atomic Force Microscope probe. (a-d) SEM images of an AFM probe (Courtesy: Nanosensors) and (e-f) different parts of AFM probe

1.2.2 State of the Art in Pull-in Voltage modeling of an AFM Probe

There has been very little published work available in the public domain that pursued to develop some closed-form readily usable analytical method to determine the pull-in voltage and the pull-in distance associated with an AFM probe. There are existing models for the electrostatic bending of cantilevers and microstructures as well as models for determining the pull-in voltage of those structures. The authors in [13] have presented a closed-form model for the pull-in voltage of electrostatically actuated cantilever beams. The cantilever structure which has been considered in [13] is shown in figure 3 redrawn from [13]. The authors in [14] have presented closed-form solutions for the pull-in voltage of micro curled beams subjected to electrostatic loads. The structure which has been considered in [14] is shown in figure 4 redrawn from [14]. Both of these models do not include the effect of the AFM probe tip and the inclination angle of the AFM probe cantilever.

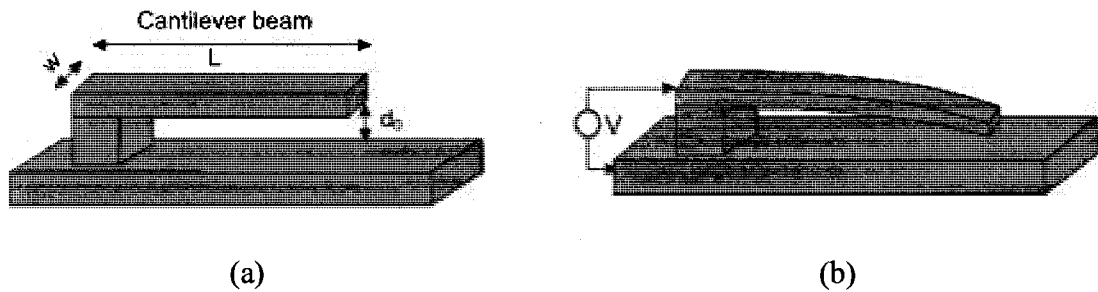


Figure 3. Microfabricated cantilever beam [13]. (a) Before pull-in, (b) After pull-in.

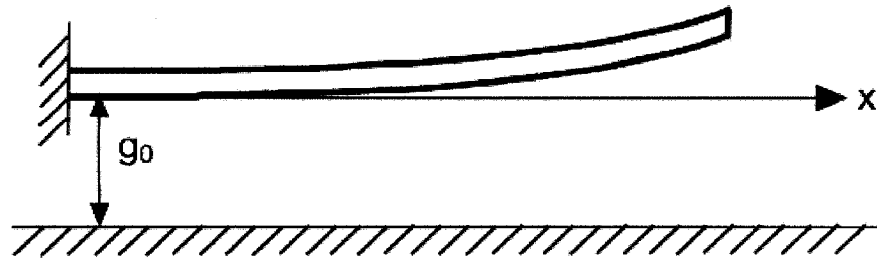


Figure 4. A curled beam [14].

There are existing models for the electrostatic bending of AFM probe under electrostatic operation [15-16] which did not include the pull-in events of the probe onto the surface under it. In [12], the authors presented a curve model to predict the pull-in voltage of an AFM probe considering the real geometric specifications and operating conditions. This curve model needs some parameter to be extracted from experimentally determined values to be able to predict the pull-in voltage of AFM probe. Figure 5 shows a schematic diagram of the AFM probe model used in [12].

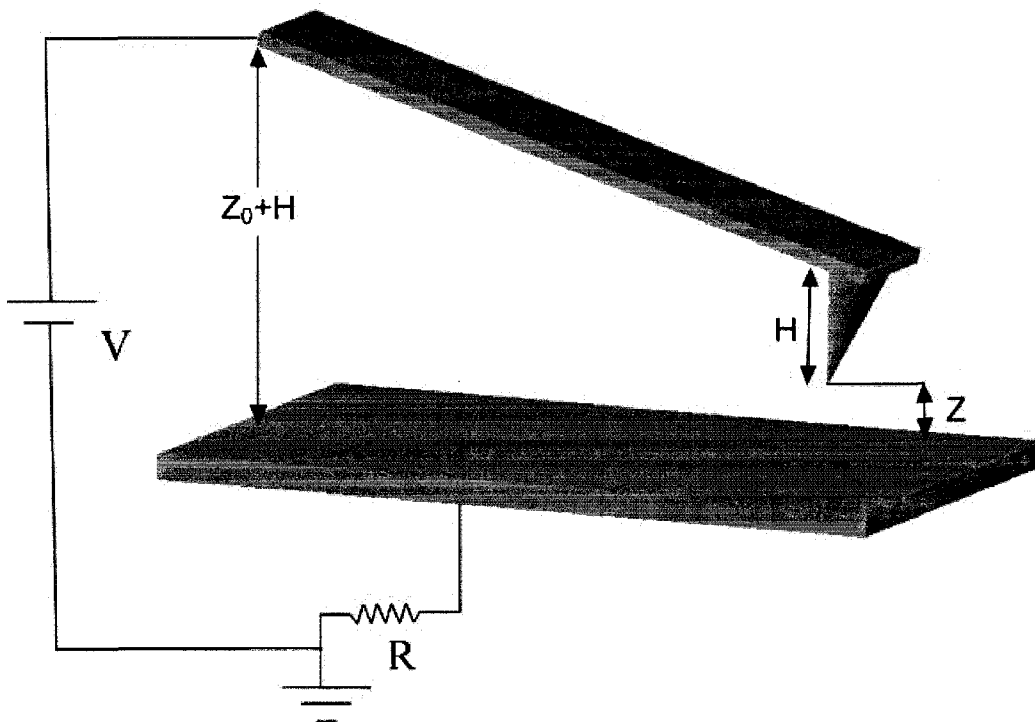


Figure 5. A schematic diagram of the AFM probe model used in [12] showing parameter notations.

In figure 5, z is the instantaneous distance between the spherical tip apex and substrate, z_0 is the initial distance between the spherical tip apex and substrate, H is the height of the tip cone, and V is the applied bias voltage.

Following [12], the instantaneous deflection of the probe can be expressed as:

$$z_0 - z = \frac{(F + f(z))}{2K} V \quad (1)$$

The pull-in distance vs. initial distance curve model can be expressed as:

$$z_0 - z_c = \frac{F + f(z_c)}{-f'(z_c)} \quad (2)$$

And finally the pull-in voltage vs. pull-in distance curve model can be expressed as:

$$V_c = \sqrt{\frac{2K}{-f'(z_c)}} \quad (3)$$

where,

$$f(z) = \frac{ab}{(z+b)z} \quad (4)$$

$$a = 2\pi\epsilon_0 R \quad (5)$$

$$b = R(1 - \sin(\theta_{cone})) \quad (6)$$

In equation (1) to (6), z_c represents the distance between the spherical tip apex and substrate at which the irreversible pull-in event occurs, K represents the spring constant of the cantilever beam, F represents the space derivative of the capacitance associated with the cantilever and tip cone with respect to the substrate, R represents the radius of

spherical tip apex, θ_{cone} represents the half opening angle of tip cone, and ϵ_0 represents the permittivity of free space.

The developed curve models in [12] need to extract some parameters F , K , a , and b from experimental results for a single initial distance between the spherical tip apex and the substrate. By plugging those values in equation (2) and (3) one can generate the desired initial distance z_0 vs. pull-in voltage V_c curve. The method isn't straight forward as for every different AFM probe geometry, an experimental measurement must be carried out first to extract the mentioned parameter values and the model can predict the pull-in voltage values only based on those values.

1.2.3 Limitations of Existing Models

The limitations of the existing models available in the literature can be addressed as followings:

- Models for cantilevers and microstructures do not include the effect of the AFM probe tip and the inclination angle of the AFM probe cantilever.
- The only model that considers the real geometric and operating conditions of AFM probe needs to extract some parameters from experimentally determined values.
- Does not offer the opportunity to observe the influence of the geometrical and other parameters of an AFM probe on pull-in voltage and load-deflection characteristic
- Don't include the force associated with the fringing field capacitances

1.3 Scientific Approach to Solve the Problem

The development sequence of the closed-form analytical model to predict the pull-in voltage of an AFM probe is listed below:

1. Investigation of the literature to find out mathematical models for different forces (Electrostatic, van der Waals etc), capacitances between AFM probe and the substrate under it, stiffness parameter associated with AFM probe and differential equations that govern the load-deflection characteristics of such beam.
2. Development of a model of the energy content of the AFM probe-substrate system.
3. Determination of the minimum energy of the system to determine the stable equilibrium point.
4. Determination of the inflection point.
5. Solving the equation set for the energy content of the system at the inflection point will yield a closed-form mathematical expression for the pull-in voltage.

1.4 Principal Results

The principal results of this research work are stated below:

1. A highly accurate analytical model for the electrostatic energy in Atomic Force Microscope probe-substrate has been developed
2. A readily computable closed-form analytical model for the pull-in voltage of an Atomic Force Microscope probe has been developed.
3. The model has been verified by comparing the pull-in voltage results predicted by the developed model with some experimentally determined results available in [12]. The developed model is found to be in excellent agreement with minimum deviation of 0.59% and maximum deviation of 3.36 % from the experimental results.

4. The new model is also in very much agreement with the finite element analysis results using IntelliSuite™ having a maximum deviation of 9.57 % for one probe and 3.05% for another probe. Investigation shows that this apparent large deviation of pull-in voltage for former probe predicted by new model and finite element analysis results is due to minimum mesh size mismatch between the spherical tip apex and the substrate underneath and is a limitation of IntelliSuite software
5. The model maintains its accuracy consistently over a wide range of initial gap between the spherical tip apex and the substrate underneath when compared with experimental and curve model predicted values.
6. The model provides an easy and readily computable method to calculate the pull-in voltage of an AFM probe compared to a model presented elsewhere where it is necessary to use some experimentally determined values to be used for the calculation.

1.5 Organization of Thesis

Chapter 2 of this thesis describes the geometric conceptions and the considerations that have been taken into account for the development of electrostatic energy in the AFM probe-substrate system and the closed-form analytical model to determine the pull-in voltage of an AFM probe. Taking these considerations into account, chapter 3 develops a mathematical expression to calculate the electrostatic energy content of the AFM probe-substrate system. In chapter 3 the effect of the fringing field capacitances between the AMF probe cantilever and substrate has been included to develop a highly accurate electrostatic energy model. Chapter 4 then presents the total energy in the AFM probe-substrate system. This chapter then describes the deflection characteristics of an AFM probe under electrostatic loads. This chapter also covers the mathematical operations necessary to develop the closed-form analytical model to predict the pull-in voltage for AFM probe. At the end of chapter 4 the final closed-form analytical model for pull-in voltage has been developed. Chapter 5 describes the construction of 3-D solid models and

meshing strategy of Atomic Force Microscope probe-substrate system using IntelliSuite™. This chapter details the difficulties associated with the construction, meshing strategy, and 3-D electromechanical finite element analysis (FEA) of the AFM probe-substrate system to determine the pull-in voltage. Chapter 6 describes the verification of the closed-form analytical model of the pull-in voltage of AFM probe developed in chapter 4 by comparing the model predicted results for different AFM probe geometries with varying initial gaps with some published experimentally determined values as well as with the results from another published curve model. The new model predicted values have also been compared with the results obtained from the 3-D electromechanical finite element analysis results using IntelliSuite. The developed model is found to be in excellent agreement with the experimental and the curve model published elsewhere as well as with FEA results

The conclusion section remarks about the fundamental observations and achievement of this research work and establishes its future directions in two senses; firstly comparing the model with more experimental results and secondly including some considerations that has been neglected to develop the model.

CHAPTER 2

DEVICE MODELING CONSIDERATIONS

This chapter deals with the fundamental geometric configuration, assumptions, and scope of this research work to develop a highly accurate model of energy content of an Atomic Force Microscope probe. The energy model later has been used to develop a closed-form model of the pull-in voltage associated with the system.

2.1 Geometry of an Atomic Force Microscope probe

An AFM probe consists of an inclined cantilever beam with a quasi-conical or pyramidal tip cone having a spherical tip apex. The AFM probe cantilever can be characterized by a length L , width w and thickness t as shown in figure 6. The tip cone height is H and θ corresponds to the half opening angle of the tip cone as shown in figure 7. The spherical tip apex has a radius R . In typical setup, the AFM probe cantilever is inclined with respect to the sample or substrate plane with an inclination angle β_{lever} as shown in figure 7.

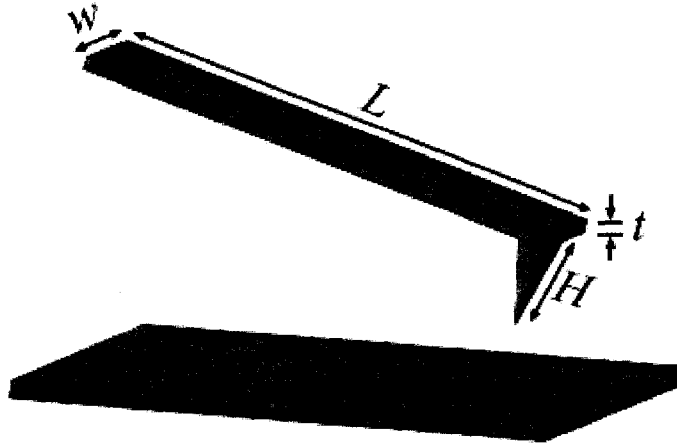


Figure 6. A schematic diagram of AFM probe-substrate system showing the cantilever length L , width w , thickness t and the height of the cone H .

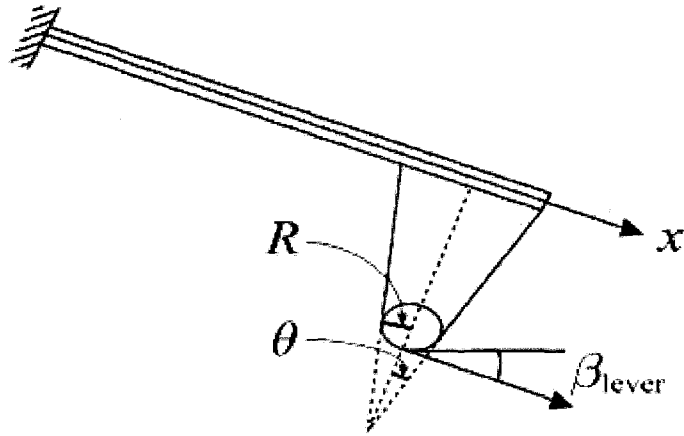


Figure 7. A line diagram of the AFM probe showing the radius R of the spherical apex of the cone, half opening angel θ of the cone, and the inclination angel β_{lever} of the cantilever with respect to substrate plane.

2.2 Energy of AFM Probe-Substrate System

In electrostatic operation the deflection profile of an AFM probe depends on various forces such as electrostatic forces F_e due to the bias voltage, van der Waals short range interaction forces F_{vdw} , and cantilever mechanical restoring force F_m . The AFM probe-substrate system is schematically shown in figure 8 together with the forces acting on the probe.

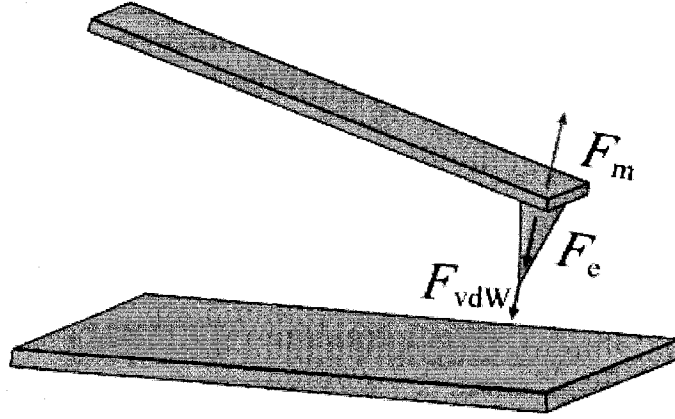


Figure 8. A schematic diagram of AFM probe-substrate system showing different forces acting on AFM probe.

The total energy of the AFM probe-substrate system is the algebraic summation of the energies associated with different force components as shown in figure 8 and can be expressed as:

$$E_T = E_m - E_e - E_{vdw} \quad (7)$$

where E_e represents energy associated with electrostatic force, E_{vdw} represents energy associated with van der Waals forces and E_m represents energy associated with cantilever mechanical restoring force.

2.2.1 Mechanical Bending Energy

The mechanical strain energy of the AFM probe-substrate system can be expressed as:

$$E_m = \int_0^L \frac{\tilde{E}I}{2} \left(\frac{d^2 \hat{w}}{dx^2} \right)^2 dx \quad (8)$$

where \tilde{E} , I , L , and \hat{w} represent effective Young's modulus, cross sectional area moment of inertia, beam length, and beam deflection as a function of axial position x , respectively. Effective Young's modulus \tilde{E} is equal to the plate modulus $E/(1-\nu^2)$ for wide beams ($w \geq 5t$), where E , and ν represent the Young's modulus and Poisson's ratio of the beam material, respectively and w , and t represent the beam width and thickness, respectively. For narrow beams \tilde{E} simply becomes the Young's modulus E . Equation (8) is based on the assumption of Euler-Bernoulli cantilever beam which requires that $L \gg w$ and $L \gg t$. AFM cantilevers beams are usually wide and fall into Euler-Bernoulli limit.

2.2.2 Electrostatic Energy

The electrostatic energy of the AFM probe-substrate system E_e can be expressed as:

$$E_e = \frac{1}{2} C_T V^2 \quad (9)$$

where C_T is the total capacitance associated with the AFM probe and the substrate system and V represents the applied bias voltage. The total capacitance C_T can be expressed as:

$$C_T = C_{lever} + C_{cone} + C_{apex} \quad (10)$$

where C_{lever} , C_{cone} , and C_{apex} represent the capacitances between the cantilever beam and substrate, the capacitances between the tip cone and substrate, and the capacitances between the spherical tip apex and substrate respectively as shown in figure 9.

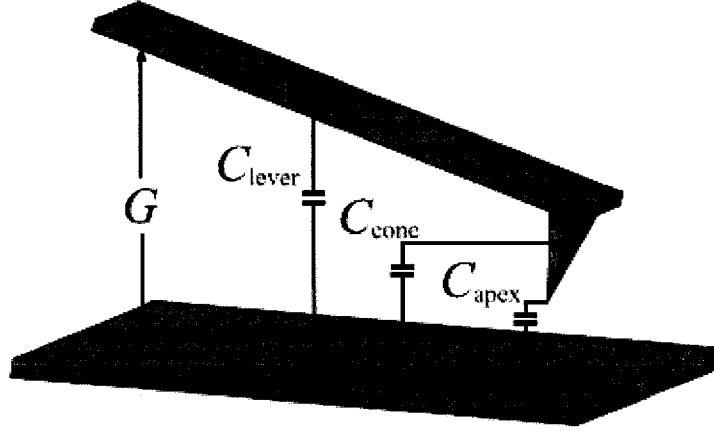


Figure 9. A schematic diagram of the AFM probe-substrate system showing various capacitance components.

2.2.3 Van der Waals Energy

Following [17], the van der Waals energy of the AFM probe-substrate system can be expressed as:

$$E_{vdw} = \frac{A}{30} \left\{ \frac{(1 + \tan^2 \theta)}{z + R(1 - \sin \theta)} + \frac{R - z}{z^2} \right\} \quad (11)$$

where A is the Hamakar constant which depends on the material properties of the tip apex of AFM probe and z is the distance between the tip apex and the substrate.

Van der Waals force becomes negligible when the distance between AFM tip and substrate is more than a few nanometers [18]. As the collapse of the AFM probe due to the electrostatic force takes place at a much higher distance between the AFM tip and the substrate, in typical analysis the energy associated with the van der Waals force is neglected. Accordingly, this analysis is focused on the investigation of the probe collapse due to the electrostatic and the mechanical restoring energies only.

Chapter summary

In this chapter the fundamental geometrical configuration of an AFM probe-substrate system has been presented. The considerations and assumptions that have been taken into account for the development of the closed-form analytical model to determine the pull-in voltage of an AFM probe are also presented. As the first step of the model development, different capacitances, forces, and energies associated with these different forces have been identified. Then the mathematical expressions for different energies, such as van der Waals energy, mechanical bending energy, and electrostatic energy are presented. These mathematical expressions are used in the next chapter to develop a more accurate model of the electrostatic energy associated with the system.

CHAPTER 3

ELECTROSTATIC ENERGY MODELING

This chapter develops a more accurate model of the electrostatic energy stored in the AFM probe-substrate system after applying a bias voltage. At first a capacitance model has been developed to determine the capacitance between the AFM probe cantilever and substrate. The capacitance model takes account of the fringing field capacitances associated with the cantilever to realize a more accurate energy expression for the system as the fringing field capacitances were neglected so far in the published literature while deriving the energy stored in an AFM probe-substrate system. This chapter also presents capacitance models associated with AFM probe tip cone and tip apex. And finally all the capacitance models have been used to derive a more accurate electrostatic energy model for an AFM probe-substrate system.

3.1 Capacitance Associated with AFM Probe cantilever

In a typical geometry, the cantilever beam of an AFM probe-substrate system is inclined at an angle β_{lever} with respect to substrate plane as shown in figure 10. Since the gap between the cantilever and the substrate is variable along the beam axis, following [18-19] the capacitance between the AFM probe cantilever and the substrate can be expressed as:

$$C_{lever} = \epsilon_0 \int_0^L \frac{w}{g(x)} dx \quad (12)$$

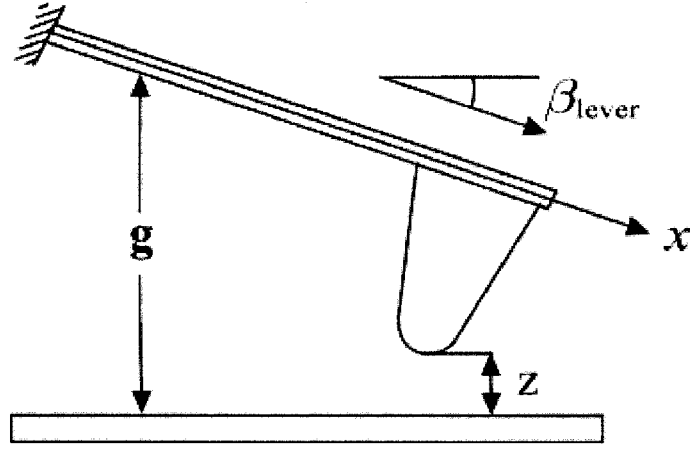


Figure 10. Schematic diagram of AFM probe cantilever arrangement.

where $g(x)$ is the variable gap between cantilever and substrate and can be expressed as:

$$g(x) = z + H\cos\beta_{lever} + L\sin\beta_{lever} - x\sin\beta_{lever} \quad (13)$$

where z is the distance between the tip apex and the substrate.

Another model [12, 20] expresses the capacitance between the AFM probe cantilever and the substrate as:

$$C_{lever} = \frac{\epsilon_0 w \tan^2(\beta_{lever})}{\beta_{lever}^2 \tan(\frac{\beta_{lever}}{2})} \ln\left(1 + \frac{2L \tan(\beta_{lever} / 2)}{z + H}\right) \quad (14)$$

Both of these models have neglected the fringing field capacitance between the cantilever and substrate. However, as the fringing field capacitance becomes a significant contributor to the stored electrostatic energy if the beam is narrow [22], a capacitance model that includes the fringing field effects is necessary for higher level of accuracy.

However, there is no straight-forward accurate analytical solution is available to compute the fringing field capacitance associated with a beam-substrate system except computationally highly expensive numerical methods. However, some approximate closed-form models are available in literature that can calculate the total capacitance including the fringing field capacitance of a VLSI on-chip interconnect separated from the substrate by a thin dielectric material. Since a square cross-section beam separated from a fixed ground plane by a thin airgap and a VLSI on-chip interconnect separated from the substrate by a thin dielectric has similar geometric configuration, models for computing the capacitance associated with a VLSI on-chip interconnect can readily be adopted to determine the capacitance associated with a beam-airgap-substrate system. A conformal transformation method has been used in [23] to derive relatively simpler equations to compute the capacitance of a long straight rectangular cross-section VLSI on-chip interconnects. The method—known as the Chang’s formula—is considered the most accurate closed-form method to date [24] and the accuracy is within 1% of the values as numerically computed in [25] as long as $w \geq d_0$ holds where d_0 is the gap between the interconnect and substrate. However, the method is computationally more expensive when compared to the methods proposed in [26-28]. Excellent comparison of the above methods regarding accuracy and computation time is available in [24] where it was determined that Meijs and Fokkema’s method proposed in [26] is superior to the methods proposed in [26-27] in terms of accuracy, validity range, and speed. It has been determined that the maximum deviation of Meijs and Fokkema’s method from the one developed by Chang is 2% when $w/d_0 \geq 1$, $0.1 \leq h/d_0 \leq 4$ and 6% as long as $w/d_0 \geq 0.3$, $h/d_0 \leq 10$ holds [26]. On the basis of these considerations, the formula proposed by Meijs and Fokkema has been adopted for this analysis.

Following [26], the capacitance between a VLSI on-chip interconnects separated from the substrate by a dielectric medium can be expressed as:

$$C = \varepsilon_0 \varepsilon_r \left[\left(\frac{w}{G} \right) + 0.77 + 1.06 \left(\frac{w}{G} \right)^{0.25} + 1.06 \left(\frac{t}{G} \right)^{0.5} \right] \quad (15)$$

where the first term on the right hand side of (15) is the parallel plate capacitance, second term is an length dependent adjustment parameter, third term is the fringing field capacitance due to interconnect width, and the fourth term is the fringing field capacitance due to interconnect thickness. In (15) ϵ_0 and ϵ_r represents the permittivity of free space and the relative permittivity of the dielectric spacer, respectively.

As for the AFM probe geometry, the gap between the inclined beam and the substrate isn't uniform, (15) cannot be used readily to determine the capacitance between an AFM probe cantilever and the substrate. However, the nonuniform gap along the axial direction of the beam can be incorporated in (8) to calculate C_{lever} as:

$$C_{lever} = \int_0^L \epsilon_0 \left\{ \left(\frac{w}{G - \hat{w}} \right) + 0.77 + 1.06 \left(\frac{w}{G - \hat{w}} \right)^{0.25} + 1.06 \left(\frac{t}{G - \hat{w}} \right)^{0.5} \right\} dx + \epsilon_0 1.06 w \left(\frac{t}{G - \hat{w}} \right)^{0.5} \quad (16)$$

where G represents the initial gap between the cantilever and the substrate and can be expressed as:

$$G = \hat{w}_0 + H \cos \beta_{lever} + L \sin \beta_{lever} - x \sin \beta_{lever} \quad (17)$$

where \hat{w}_0 is the initial distance between the tip apex and the substrate. The last term in (16) is the fringing field capacitance at the free end of the cantilever.

3.2 Capacitance Associated with AFM Tip Cone

Following [30], the capacitance associated with the tip cone and the substrate can be expressed as:

$$C_{cone} = 2\varepsilon_0 n \left[(\hat{w}_0 + b - \hat{w}) \left\{ \ln \left(\frac{\hat{w}_0 + b - \hat{w}}{H} \right) - 1 \right\} + (\hat{w}_0 - \hat{w}) - c \log(\hat{w}_0 + b - \hat{w}) \right] \quad (18)$$

where

$$\begin{cases} b = R(1 - \sin\theta), \\ c = R \frac{\cos^2\theta}{\sin\theta} \\ n = \pi q^2, \\ q^2 = [\ln\{\tan(0.5\theta)\}]^{-2} \end{cases} \quad (19)$$

The parameters b , c , n , and q are functions of radius R of the spherical tip apex and the half-opening angle θ of tip cone. These two parameters are constants for a specific AFM probe geometry.

3.3 Capacitance Associated with AFM Tip Apex

Following [30], the capacitance associated with the spherical tip apex and the substrate can be expressed as:

$$C_{apex} = \varepsilon_0 m \ln \left(\frac{\hat{w}_0 + b - \hat{w}}{\hat{w}_0 - \hat{w}} \right) \quad (20)$$

where m is a function which depends on the radius R of the spherical tip apex and can be expressed as:

$$m = 2\pi R \quad (21)$$

3.4 Electrostatic Energy of AFM Probe-Substrate System

The electrostatic energy stored in the AFM probe-substrate system can be calculated by using the capacitance models associated with the AFM probe cantilever, tip cone and spherical tip apex with respect to substrate. Total capacitance C_T of the system can be determined by substituting (16), (18), and (20) in (10) and the stored electrostatic energy then can be determined following (9) as:

$$\begin{aligned}
 E_e = \frac{1}{2} \varepsilon_0 V^2 & \left[\int_0^L \left\{ \left(\frac{w}{G - \hat{w}} \right) + 0.77 + 1.06 \left(\frac{w}{G - \hat{w}} \right)^{0.25} + 1.06 \left(\frac{t}{G - \hat{w}} \right)^{0.5} \right\} dx \right. \\
 & + 1.06 w \left(\frac{t}{G_{(L)} - \hat{w}} \right)^{0.5} \\
 & + 2n \left\{ (\hat{w}_0 + b - \hat{w}) \left(\ln \left(\frac{\hat{w}_0 + b - \hat{w}}{H} \right) - 1 \right) + (\hat{w}_0 - \hat{w}) - c \ln(\hat{w}_0 + b - \hat{w}) \right\} \\
 & \left. + m \ln \left(\frac{\hat{w}_0 + b - \hat{w}}{\hat{w}_0 - \hat{w}} \right) \right] \tag{22}
 \end{aligned}$$

Chapter summary

An improved model to predict the electrostatic energy in an AFM probe-substrate system has been developed by developing a new capacitance model for the capacitance between the AFM probe cantilever and substrate that includes the energy associated with the fringing field capacitances. This more accurate representation of the stored electrostatic energy is then used to develop a highly accurate closed-form model for the pull-in voltage of the AFM probe as described in the next chapter. Capacitance models associated with AFM probe tip cone and tip apex, which are necessary for calculating the electrostatic energy, have also been presented in this chapter.

CHAPTER 4

PULL-IN VOLTAGE MODELING

This chapter develops a readily computable closed-form analytical model to determine the pull-in voltage of an Atomic Force Microscope probe. At first total energy of the AFM probe-substrate system has been determined. Then the formulations for the deflection shape of an AFM probe cantilever beam under electrostatic pressure are provided. Finally the mathematical operations needed to develop the closed-form analytical model to predict the pull-in voltage for the AFM probe has been described.

4.1 Total Energy of AFM Probe-Substrate System

After biasing, the electrostatic attraction force pulls the AFM probe towards the substrate while the elastic restoring force opposes any deformation of the beam. The net force working on the beam is the algebraic summation of these two forces. Thus at equilibrium, the total energy of the AFM probe-substrate system is the net energy associated with the net force and can be derived from the expressions for the electrostatic and the mechanical restoring energies. Following this approach, using (7), (8), and (22) and neglecting the van der Waals force the total energy of the system can be expressed as:

$$\begin{aligned}
E_T = & \int_0^L \frac{\tilde{E}I}{2} \left(\frac{d^2 \hat{w}}{dx^2} \right)^2 dx \\
& - \frac{1}{2} \varepsilon_0 V^2 \left[\int_0^L \left\{ \left(\frac{w}{G - \hat{w}} \right) + 0.77 + 1.06 \left(\frac{w}{G - \hat{w}} \right)^{0.25} + 1.06 \left(\frac{t}{G - \hat{w}} \right)^{0.5} \right\} dx \right. \\
& + 1.06 w \left(\frac{t}{G_{(L)} - \hat{w}} \right)^{0.5} \\
& + 2n \left\{ (\hat{w}_0 + b - \hat{w}) \left(\ln \left(\frac{\hat{w}_0 + b - \hat{w}}{H} \right) - 1 \right) + (\hat{w}_0 - \hat{w}) - c \ln(\hat{w}_0 + b - \hat{w}) \right\} \\
& \left. + m \ln \left(\frac{\hat{w}_0 + b - \hat{w}}{\hat{w}_0 - \hat{w}} \right) \right] \tag{23}
\end{aligned}$$

The pull-in voltage can be determined from the second derivative of the total energy stored in the system. However, due to the presence of the nonlinear terms in (23), it is very difficult to derive an exact analytical solution for the pull-in voltage from (23). Investigation shows that the nonlinear terms in (23) can be linearized using the well-known Taylor series expansion method to obtain a sufficiently accurate analytical model for the desired pull-in voltage. Following this approach, expanding the nonlinear terms in (23) by Taylor series about the zero deflection position of the tip, ($\hat{w} = 0$), one obtains:

$$\begin{aligned}
E_T = & \int_0^L \frac{\tilde{E}I}{2} \left(\frac{d^2 \hat{w}}{dx^2} \right)^2 dx \\
& - \frac{1}{2} \varepsilon_0 V^2 \left[\int_0^L w \left(\frac{1}{G} + \frac{\hat{w}}{G^2} + \frac{\hat{w}^2}{G^3} + \frac{\hat{w}^3}{G^4} + \frac{\hat{w}^4}{G^5} + \frac{\hat{w}^5}{G^6} + \frac{\hat{w}^6}{G^7} \Lambda \right) dx + \int_0^L 0.77 dx \right. \\
& \left. + \int_0^L 1.06 w^{0.25} \left(\frac{1}{G^{0.25}} + \frac{0.25 \hat{w}}{G^{1.25}} + \frac{5 \hat{w}^2}{32 G^{2.25}} + \frac{15 \hat{w}^3}{128 G^{3.25}} + \frac{195 \hat{w}^4}{2048 G^{4.25}} \right) \right]
\end{aligned}$$

$$\begin{aligned}
& \left. + \frac{663\hat{w}^5}{8192G^{5.25}} + \frac{4641\hat{w}^6}{65536G^{6.25}} + \Lambda \right) dx \\
& + \int_0^L 1.06t^{0.5} \left(\frac{1}{G^{0.5}} + \frac{0.5\hat{w}}{G^{1.5}} + \frac{3\hat{w}^2}{8G^{2.5}} + \frac{5\hat{w}^3}{16G^{3.5}} + \frac{35\hat{w}^4}{128G^{4.5}} \right. \\
& \quad \left. + \frac{63\hat{w}^5}{256G^{5.5}} + \frac{231\hat{w}^6}{1024G^{6.5}} + \Lambda \right) dx \\
& + 1.06wt^{0.5} \left(\frac{1}{G_{(L)}^{0.5}} + \frac{0.5\hat{w}}{G_{(L)}^{1.5}} + \frac{3\hat{w}^2}{8G_{(L)}^{2.5}} + \frac{5\hat{w}^3}{16G_{(L)}^{3.5}} + \frac{35\hat{w}^4}{128G_{(L)}^{4.5}} \right. \\
& \quad \left. + \frac{63\hat{w}^5}{256G_{(L)}^{5.5}} + \frac{231\hat{w}^6}{1024G_{(L)}^{6.5}} + \Lambda \right) \\
& + 2n \left\{ (\hat{w}_0 + b) \left(\ln \left(\frac{\hat{w}_0 + b}{H} \right) - 1 \right) + \hat{w}_0 - c \ln(\hat{w}_0 + b) + \left(-\ln \left(\frac{\hat{w}_0 + b}{H} \right) - 1 + \frac{c}{\hat{w}_0 + b} \right) \hat{w} \right. \\
& \quad + \left(\frac{1}{2(\hat{w}_0 + b)} + \frac{c}{2(\hat{w}_0 + b)^2} \right) \hat{w}^2 + \left(\frac{1}{6(\hat{w}_0 + b)^2} + \frac{c}{3(\hat{w}_0 + b)^3} \right) \hat{w}^3 \\
& \quad + \left(\frac{1}{12(\hat{w}_0 + b)^3} + \frac{c}{4(\hat{w}_0 + b)^4} \right) \hat{w}^4 + \left(\frac{1}{20(\hat{w}_0 + b)^4} + \frac{c}{5(\hat{w}_0 + b)^5} \right) \hat{w}^5 \\
& \quad \left. + \left(\frac{1}{30(\hat{w}_0 + b)^5} + \frac{c}{6(\hat{w}_0 + b)^6} \right) \hat{w}^6 + \Lambda \right\} \\
& + m \left\{ \ln \left(\frac{\hat{w}_0 + b}{\hat{w}_0} \right) + \frac{b}{\hat{w}_0(\hat{w}_0 + b)} \hat{w} + \frac{2\hat{w}_0^2 b + b^2}{2\hat{w}_0^2(\hat{w}_0 + b)^2} \hat{w}^2 + \frac{3\hat{w}_0^2 b + 3\hat{w}_0 b^2 + b^3}{3\hat{w}_0^3(\hat{w}_0 + b)^3} \hat{w}^3 \right. \\
& \quad \left. + \frac{4\hat{w}_0^3 b + 6\hat{w}_0^2 b^2 + 4\hat{w}_0 b^3 + b^4}{4\hat{w}_0^4(\hat{w}_0 + b)^4} \hat{w}^4 + \frac{5\hat{w}_0^4 b + 10\hat{w}_0^3 b^2 + 10\hat{w}_0^2 b^3 + 5\hat{w}_0 b^4 + b^5}{5\hat{w}_0^5(\hat{w}_0 + b)^5} \hat{w}^5 \right.
\end{aligned}$$

$$+ \left. \frac{6\hat{w}_0^5 b + 15\hat{w}_0^4 b^2 + 20\hat{w}_0^3 b^3 + 15\hat{w}_0^2 b^4 + 6\hat{w}_0 b^5 + b^6}{6\hat{w}_0^6 (\hat{w}_0 + b)^6} \hat{w}^6 + \Lambda \right\} \quad (24)$$

As the contribution to the total energy from the fifth and higher order terms obtained after Taylor series expansion is several orders of lower magnitude compared to the initial terms, truncating the fifth and higher order terms in (24) won't introduce significant error while result in a more compact and easier energy expression. After truncating the fifth and higher order terms in (24), one obtains:

$$\begin{aligned} E_T = & \int_0^L \frac{\tilde{E}I}{2} \left(\frac{d^2 \hat{w}}{dx^2} \right)^2 dx \\ & - \frac{1}{2} \varepsilon_0 V^2 \left[\int_0^L w \left(\frac{1}{G} + \frac{\hat{w}}{G^2} + \frac{\hat{w}^2}{G^3} + \frac{\hat{w}^3}{G^4} + \frac{\hat{w}^4}{G^5} \right) dx + \int_0^L 0.77 dx \right. \\ & + \int_0^L 1.06 w^{0.25} \left(\frac{1}{G^{0.25}} + \frac{0.25 \hat{w}}{G^{1.25}} + \frac{5 \hat{w}^2}{32 G^{2.25}} + \frac{15 \hat{w}^3}{128 G^{3.25}} + \frac{195 \hat{w}^4}{2048 G^{4.25}} \right) dx \\ & + \int_0^L 1.06 t^{0.5} \left(\frac{1}{G^{0.5}} + \frac{0.5 \hat{w}}{G^{1.5}} + \frac{3 \hat{w}^2}{8 G^{2.5}} + \frac{5 \hat{w}^3}{16 G^{3.5}} + \frac{35 \hat{w}^4}{128 G^{4.5}} \right) dx \\ & + 1.06 w t^{0.5} \left\{ \frac{1}{G_{(L)}^{0.5}} + \frac{0.5 \hat{w}}{G_{(L)}^{1.5}} + \frac{3 \hat{w}^2}{8 G_{(L)}^{2.5}} + \frac{5 \hat{w}^3}{16 G_{(L)}^{3.5}} + \frac{35 \hat{w}^4}{128 G_{(L)}^{4.5}} \right\} \\ & + 2n \left\{ (\hat{w}_0 + b) \left(\ln \left(\frac{\hat{w}_0 + b}{H} \right) - 1 \right) + \hat{w}_0 - c \ln(\hat{w}_0 + b) + \left(-\ln \left(\frac{\hat{w}_0 + b}{H} \right) - 1 + \frac{c}{\hat{w}_0 + b} \right) \hat{w} \right. \\ & + \left(\frac{1}{2(\hat{w}_0 + b)} + \frac{c}{2(\hat{w}_0 + b)^2} \right) \hat{w}^2 + \left(\frac{1}{6(\hat{w}_0 + b)^2} + \frac{c}{3(\hat{w}_0 + b)^3} \right) \hat{w}^3 \\ & \left. + \left(\frac{1}{12(\hat{w}_0 + b)^3} + \frac{c}{4(\hat{w}_0 + b)^4} \right) \hat{w}^4 \right\} \end{aligned}$$

$$\begin{aligned}
& + m \left\{ \ln \left(\frac{\hat{w}_0 + b}{\hat{w}_0} \right) + \frac{b}{\hat{w}_0(\hat{w}_0 + b)} \hat{w} + \frac{2\hat{w}_0^2 b + b^2}{2\hat{w}_0^2(\hat{w}_0 + b)^2} \hat{w}^2 + \frac{3\hat{w}_0^2 b + 3\hat{w}_0 b^2 + b^3}{3\hat{w}_0^3(\hat{w}_0 + b)^3} \hat{w}^3 \right. \\
& \left. + \frac{4\hat{w}_0^3 b + 6\hat{w}_0^2 b^2 + 4\hat{w}_0 b^3 + b^4}{4\hat{w}_0^4(\hat{w}_0 + b)^4} \hat{w}^4 \right\} \quad (25)
\end{aligned}$$

4.2 Pull-in Voltage Closed-Form Model

The deflection profile function of a cantilever beam can be expressed as [31-32]:

$$\hat{w}(x) = \sum_{n=1}^{\infty} P_n \varphi_n(x) \quad (26)$$

where $\varphi_n(x)$ is the n th assumed deflection shape function that satisfies the boundary conditions and the coefficients P_n are the weighting of the associated mode that are to be determined. For free vibration of structures, the natural mode approach provides the exact solution to the vibrational amplitude and deformation shape as it satisfies the boundary conditions and the homogenous part of the governing equation of a dynamic system [33]. The natural mode approach also provides the foundation for forced response calculation in structural dynamics [33]. Moreover, as the electrostatic force due to the biasing voltage attracts the beam towards the ground plane; this kind of deformation is similar to the first natural mode of the beam. These considerations prompt to choose the first natural mode of cantilever beam as the deflection shape function.

Following [31-32], the first natural mode of a cantilever beam can be expressed as:

$$\varphi_1(x) = [\cosh(k_1 x) - \cos(k_1 x)] - \left[\frac{\sinh(k_1 L) - \sin(k_1 L)}{\cosh(k_1 L) + \cos(k_1 L)} \right] [\sinh(k_1 x) - \sin(k_1 x)] \quad (27)$$

where the coefficient k_1 represents the flexural wave number of the first natural mode and satisfies the following relation:

$$\cosh(k_1 L) \cos(k_1 L) = -1 \quad (29)$$

In (29) $k_1 L \approx 1.875$ is the wave number of first natural mode times the length of the cantilever. Substituting (27) in (26) the deflection function of the AFM probe cantilever can be given by:

$$\hat{w}(x) = P_1 \varphi_1(x) \quad (30)$$

where P_1 is the weighting of the first natural mode that is to be determined. Renaming P_1 and $\varphi_1(x)$ as P and $\varphi(x)$, respectively, (30) can be re-written as

$$\hat{w}(x) = P\varphi(x) \quad (31)$$

The total energy E_T of the AFM probe-substrate system thus can be expressed in terms of P and $\varphi(x)$ by substituting (31) in (25) as:

$$E_T = \int_0^L \frac{\tilde{E}I}{2} (P\varphi'')^2 dx$$

$$- \frac{1}{2} \varepsilon_0 V^2 \left[\int_0^L w \left(\frac{1}{G} + \frac{P\varphi}{G^2} + \frac{(P\varphi)^2}{G^3} + \frac{(P\varphi)^3}{G^4} + \frac{(P\varphi)^4}{G^5} \right) dx \right]$$

$$+ \int_0^L 1.06w^{0.25} \left(\frac{1}{G^{0.25}} + \frac{0.25P\varphi}{G^{1.25}} + \frac{5(P\varphi)^2}{32G^{2.25}} + \frac{15(P\varphi)^3}{128G^{3.25}} + \frac{195(P\varphi)^4}{2048G^{4.25}} \right) dx$$

$$\begin{aligned}
& + \int_0^L 1.06t^{0.5} \left(\frac{1}{G^{0.5}} + \frac{0.5P\varphi}{G^{1.5}} + \frac{3(P\varphi)^2}{8G^{2.5}} + \frac{5(P\varphi)^3}{16G^{3.5}} + \frac{35(P\varphi)^4}{128G^{4.5}} \right) dx \\
& + 1.06wt^{0.5} \left(\frac{1}{G_{(L)}^{0.5}} + \frac{0.5P\varphi_{(L)}}{G_{(L)}^{1.5}} + \frac{3(P\varphi_{(L)})^2}{8G_{(L)}^{2.5}} + \frac{5(P\varphi_{(L)})^3}{16G_{(L)}^{3.5}} + \frac{35(P\varphi_{(L)})^4}{128G_{(L)}^{4.5}} \right) \\
& + 2n \left\{ (\hat{w}_0 + b) \ln \left(\frac{\hat{w}_0 + b}{H} \right) - b - c \ln(\hat{w}_0 + b) + \left(-\ln \left(\frac{\hat{w}_0 + b}{H} \right) - 1 + \frac{c}{\hat{w}_0 + b} \right) P\varphi_{(L)} \right. \\
& + \left(\frac{1}{2(\hat{w}_0 + b)} + \frac{c}{2(\hat{w}_0 + b)^2} \right) (P\varphi_{(L)})^2 + \left(\frac{1}{6(\hat{w}_0 + b)^2} + \frac{c}{3(\hat{w}_0 + b)^3} \right) (P\varphi_{(L)})^3 \\
& + \left. \left(\frac{1}{12(\hat{w}_0 + b)^3} + \frac{c}{4(\hat{w}_0 + b)^4} \right) (P\varphi_{(L)})^4 \right\} \\
& + m \left\{ \log \left(\frac{\hat{w}_0 + b}{\hat{w}_0} \right) + \frac{b}{\hat{w}_0(\hat{w}_0 + b)} P\varphi_{(L)} + \frac{2\hat{w}_0^2 b + b^2}{2\hat{w}_0^2(\hat{w}_0 + b)^2} (P\varphi_{(L)})^2 \right. \\
& + \left. \frac{3\hat{w}_0^2 b + 3\hat{w}_0 b^2 + b^3}{3\hat{w}_0^3(\hat{w}_0 + b)^3} (P\varphi_{(L)})^3 + \frac{4\hat{w}_0^3 b + 6\hat{w}_0^2 b^2 + 4\hat{w}_0 b^3 + b^4}{4\hat{w}_0^4(\hat{w}_0 + b)^4} (P\varphi_{(L)})^4 \right\} \quad (32)
\end{aligned}$$

Rearranging (32),

$$E_T = \int_0^L \frac{\tilde{E}I}{2} (P\varphi'')^2 dx - \frac{1}{2} \varepsilon_0 V^2 (A_0 + A_1 P + A_2 P^2 + A_3 P^3 + A_4 P^4) \quad (33)$$

where

$$A_0 = \int_0^L \left(\frac{w}{G} + 0.77 + \frac{1.06w^{0.25}}{G^{0.25}} + \frac{1.06t^{0.5}}{G^{0.5}} \right) dx + \frac{1.06wt^{0.5}}{G_{(L)}^{0.5}} + 2n \left\{ (\hat{w}_0 + b) \ln \left(\frac{\hat{w}_0 + b}{H} \right) - b - c \ln(\hat{w}_0 + b) \right\} + m \left\{ \ln \left(\frac{\hat{w}_0 + b}{\hat{w}_0} \right) \right\} \quad (34)$$

$$A_1 = \int_0^L \left[\left(\frac{w}{G^2} + \frac{0.265w^{0.25}}{G^{1.25}} + \frac{0.53t^{0.5}}{G^{1.5}} \right) \varphi dx \right] + \left[\frac{0.53wt^{0.5}}{G_{(L)}^{1.5}} + 2n \left\{ -\ln \left(\frac{\hat{w}_0 + b}{H} \right) - 1 + \frac{c}{\hat{w}_0 + b} \right\} + m \left\{ \frac{b}{\hat{w}_0(\hat{w}_0 + b)} \right\} \right] \varphi_{(L)} \quad (35)$$

$$A_2 = \int_0^L \left[\left(\frac{w}{G^3} + \frac{5.3w^{0.25}}{32G^{2.25}} + \frac{3.18t^{0.5}}{8G^{2.5}} \right) \varphi^2 dx \right] + \left[\frac{3.18wt^{0.5}}{8G_{(L)}^{2.5}} + 2n \left\{ \frac{1}{2(\hat{w}_0 + b)} + \frac{c}{2(\hat{w}_0 + b)^2} \right\} + m \left\{ \frac{2\hat{w}_0^2 b + b^2}{2\hat{w}_0^2(\hat{w}_0 + b)^2} \right\} \right] \varphi^2_{(L)} \quad (36)$$

$$A_3 = \int_0^L \left[\left(\frac{w}{G^4} + \frac{15.9w^{0.25}}{128G^{3.25}} + \frac{5.3t^{0.5}}{16G^{3.5}} \right) \varphi^3 dx \right] + \left[\frac{5.3wt^{0.5}}{16G_{(L)}^{3.5}} + 2n \left\{ \frac{1}{6(\hat{w}_0 + b)^2} + \frac{c}{3(\hat{w}_0 + b)^3} \right\} + m \left\{ \frac{3\hat{w}_0^2 b + 3\hat{w}_0 b^2 + b^3}{3\hat{w}_0^3(\hat{w}_0 + b)^3} \right\} \right] \varphi^3_{(L)} \quad (37)$$

$$A_4 = \int_0^L \left[\left(\frac{w}{G^5} + \frac{206.7w^{0.25}}{2048G^{4.25}} + \frac{37.1t^{0.5}}{128G^{4.5}} \right) \varphi^4 dx \right] + \left[\frac{37.1wt^{0.5}}{128G_{(L)}^{4.5}} + 2n \left\{ \frac{1}{12(\hat{w}_0 + b)^3} + \frac{c}{4(\hat{w}_0 + b)^4} \right\} + m \left\{ \frac{4\hat{w}_0^3 b + 6\hat{w}_0^2 b^2 + 4\hat{w}_0 b^3 + b^4}{4\hat{w}_0^4(\hat{w}_0 + b)^4} \right\} \right] \varphi^4_{(L)} \quad (38)$$

The system is in a static equilibrium when the first order derivative of the total potential energy E_T with respect to the coefficient P is zero [34]. Taking the derivative of (33) one obtains after rearrangement:

$$P \int_0^L \tilde{E}I(\varphi'')^2 dx = \frac{1}{2} \varepsilon_0 V^2 (A_1 + 2A_2 P + 3A_3 P^2 + 4A_4 P^3) \quad (39)$$

Whether the system is in a stable or unstable equilibrium state is determined by the second-order derivative of the total potential E_T with respect to P . At the transition from stable to an unstable equilibrium, the second-order derivative of the total potential E_T with respect to P equals to zero, i.e. $d^2 E_T / dP^2 = 0$. Rearranging the derivative of (39) one obtains:

$$\int_0^L \tilde{E}I(\varphi'')^2 dx = \frac{1}{2} \varepsilon_0 V^2 (2A_2 + 6A_3 P + 12A_4 P^2) \quad (40)$$

Dividing (40) by (39) yields:

$$8A_4 P^3 + 3A_3 P^2 - A_1 = 0 \quad (41)$$

Equation (41) can be solved by Cardan solution [35]. Out of the three roots, two are imaginary while the real root corresponds to the value of P at pull-in and can be determined as:

$$P_{PI} = S + T - \frac{A_3}{8A_4} \quad (42)$$

where,

$$\begin{cases} S = \sqrt[3]{M + \sqrt{N^3 + M^2}}, \\ T = \sqrt[3]{M - \sqrt{N^3 + M^2}} \\ M = \frac{A_1/A_4}{16} - \frac{(A_3/A_4)^3}{512}, \\ N = -\frac{(A_3/A_4)^2}{64} \end{cases} \quad (43)$$

Substituting (42) in (40) yields the desired closed-form solution for the pull-in voltage V_{PI} as

$$V_{PI} = \sqrt{\frac{2 \int_0^L \tilde{E} I (\varphi'')^2 dx}{\epsilon_0 (2 A_2 + 6 A_3 P_{PI} + 12 A_4 P_{PI}^2)}} \quad (44)$$

Chapter summary

A readily computable closed-form analytical model to determine the pull-in voltage of an AFM probe has been developed. Taylor series expansion method has been employed to expand the electrostatic energy and higher order terms in the expansion series have been truncated to realize a more compact and easier expression of the electrostatic energy. First natural mode of the beam has been assumed as the deflection shape function of the beam. An expression for the weighting parameter associated with the first natural mode of vibration at pull-in has been derived. This expression is then substituted in the second derivative of the total energy expression. At pull-in, the second derivative of the stored energy goes to zero. This condition is then utilized to solve the second derivative of the energy expression to yield the target closed-form model for the pull-in voltage.

CHAPTER 5

FEA MODELING

In this Chapter construction of 3-D solid models and meshing strategy of Atomic Force Microscope probe-substrate system using IntelliSuite™ is presented. The chapter details the difficulties associated with the construction, meshing strategy, and 3-D electromechanical finite element analysis (FEA) of the AFM probe-substrate system to determine the pull-in voltage. The difficulties arise due to the unique geometry of the system and the mesh size conformity required by the software to accurately calculate the electrostatic force that causes the pull-in.

5.1 Construction of Atomic Force Microscope Probes

Geometric specifications of two commercially available AFM probes that were modeled using IntelliSuite™ to verify the developed pull-in voltage model are presented in table 1.

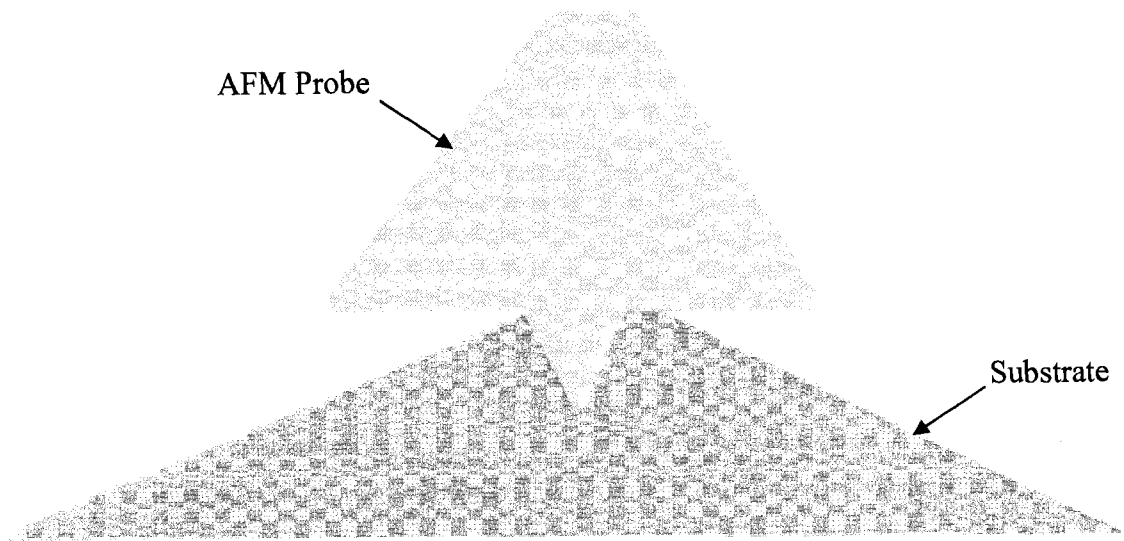
Table 1. Specifications of AFM probes

Probe	Probe 1	Probe 2
Nominal length, L (μm)	450	225
Nominal width, w (μm)	50	28
Nominal thickness, t (μm)	2	2.416
Cone height, H (μm)	17	15
Half opening angle, θ ($^\circ$)	23	9
Apex radius, R (nm)	118	146

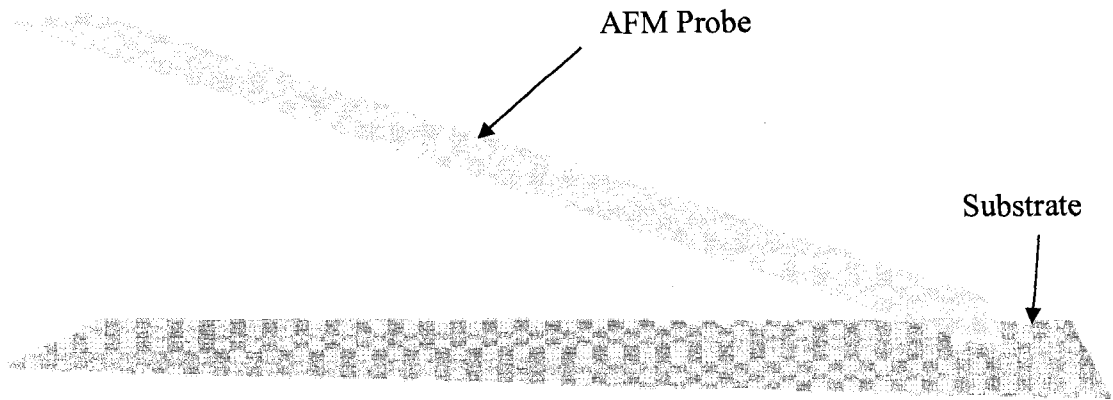
The Interactive 3D Builder is an IntelliSuite module for building and meshing the three-dimensional geometry of MEMS structures. 3D Builder module of IntelliSuite has been used to model both the Probe 1 and Probe 2. These probes present a rectangular shaped cantilever with integrated pyramidal shaped tip cone. The cantilevers are drawn with an inclination of 21° with respect to substrate.

5.1.1 Geometry of First Probe

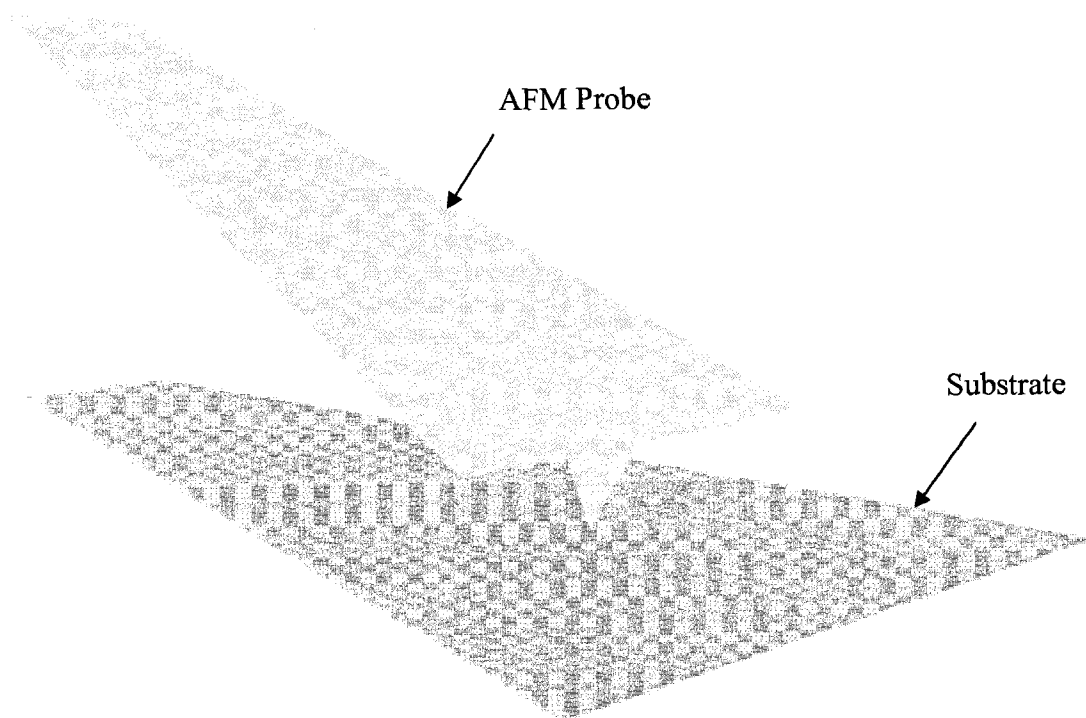
The first probe, probe 1 presents AFM probe of cantilever length of 450 micrometer (μm), width of 50 micrometer (μm) and thickness of 2 micrometer (μm). The pyramidal cone has height of 17 micrometer (μm) and of the half opening angle of 23° . The radius of the spherical apex at the end of the tips is 118 nanometers (nm). Figure 11 shows different views for the 3-D model for probe 1 that has been constructed in 3D Builder of IntelliSuite.



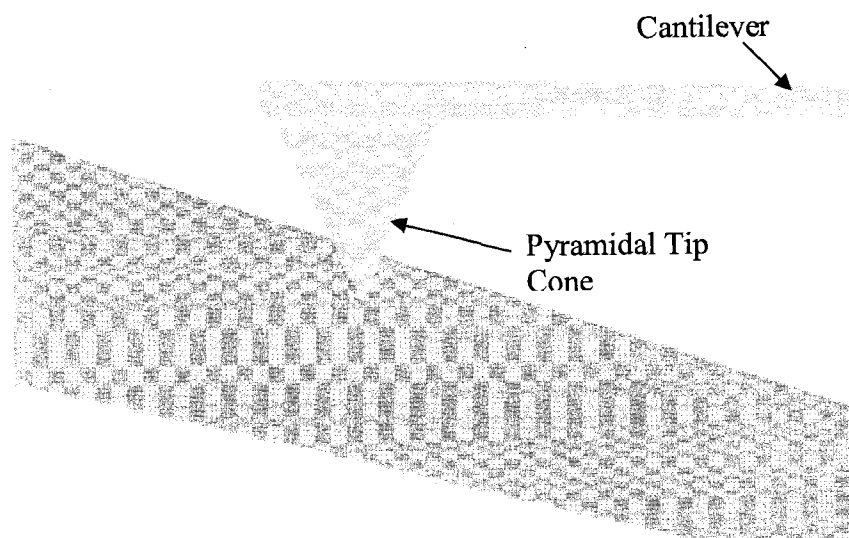
(a)



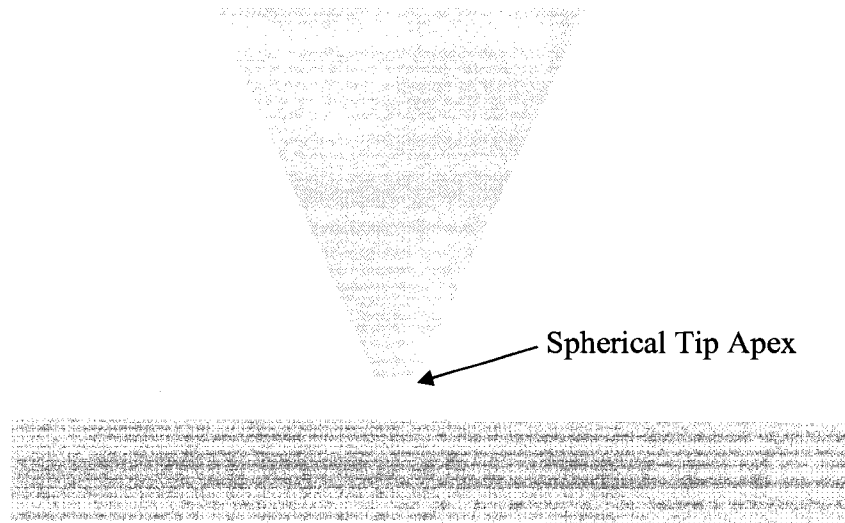
(b)



(c)



(d)

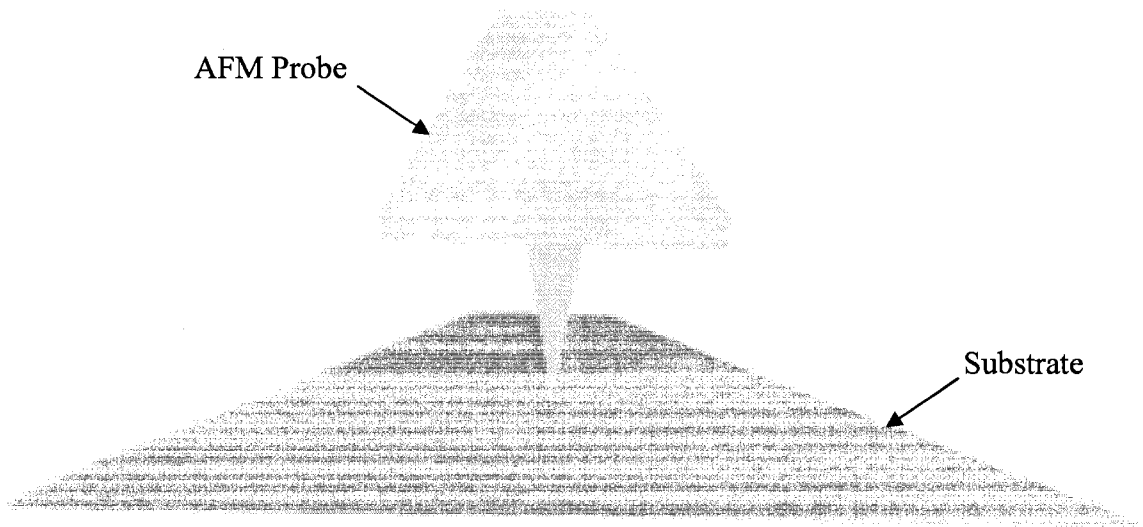


(e)

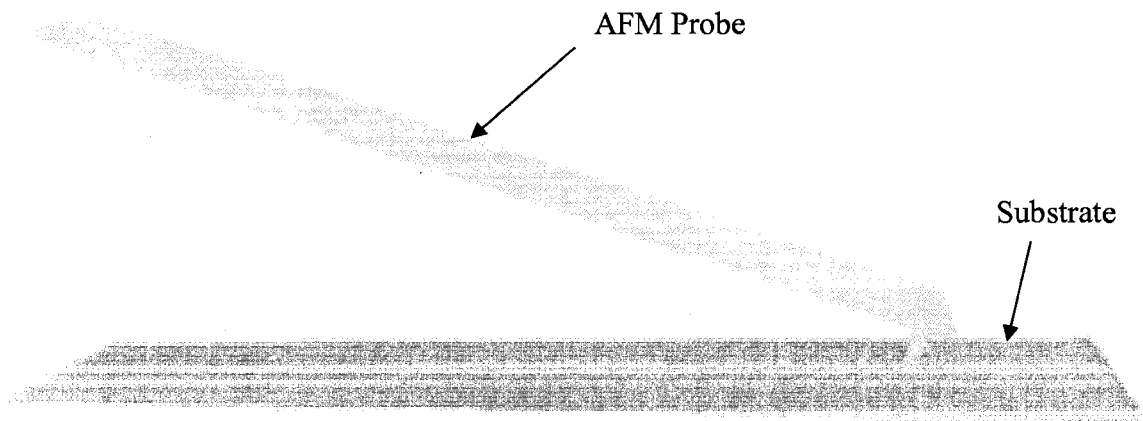
Figure 11. Geometry of AFM probe 1. (a) Front view of whole of the AFM probe-substrate system, (b) Side view of the AFM probe, (c) Orthogonal view of the AFM probe, (d) Side view of the pyramidal tip cone and the part of cantilever, (e) Spherical tip apex at the end of the tip.

5.1.2 Geometry of Second Probe

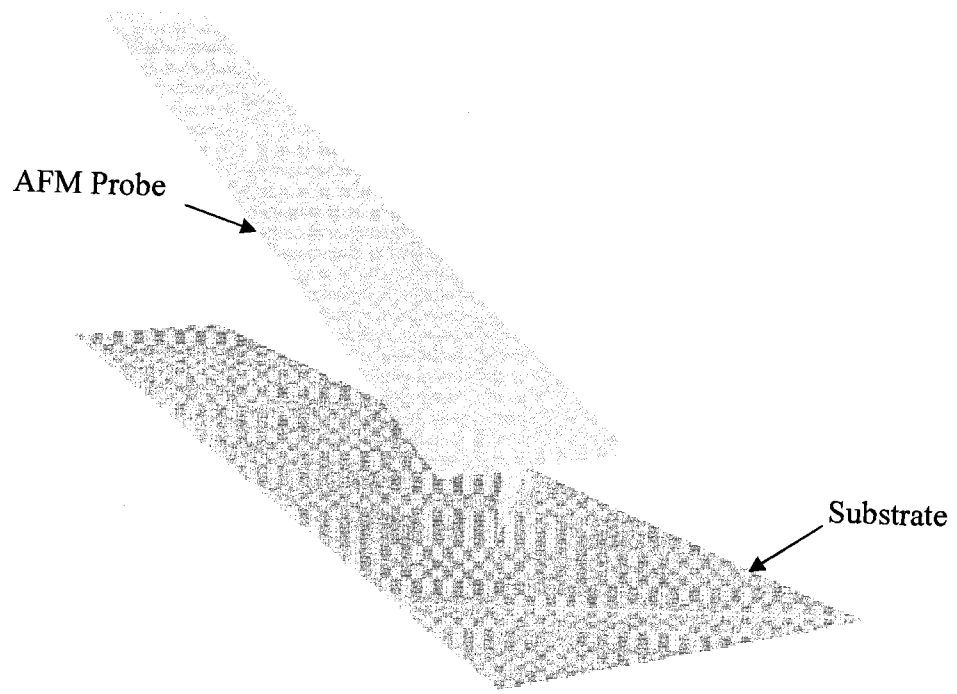
The second probe, probe 2 presents AFM probe of cantilever length of 225 micrometer (μm), width of 28 micrometer (μm) and thickness of 2.416 micrometer (μm). The pyramidal cone has height of 15 micrometer (μm) and of the half opening angle of 9° . The radius of the spherical apex at the end of the tips is 146 nanometers (nm). Figure 12 shows different views for the 3-D model for probe 2 that has been built in 3D Builder of IntelliSuite.



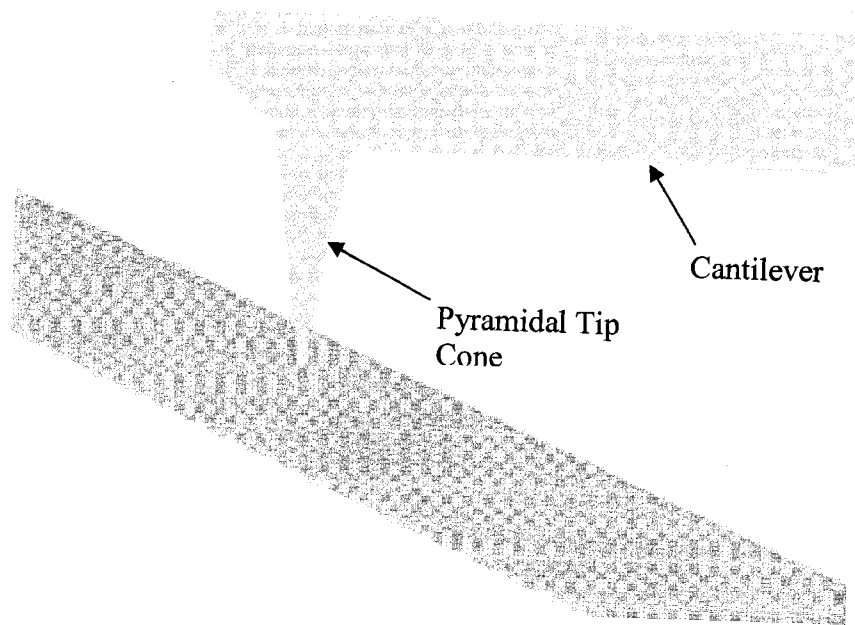
(a)



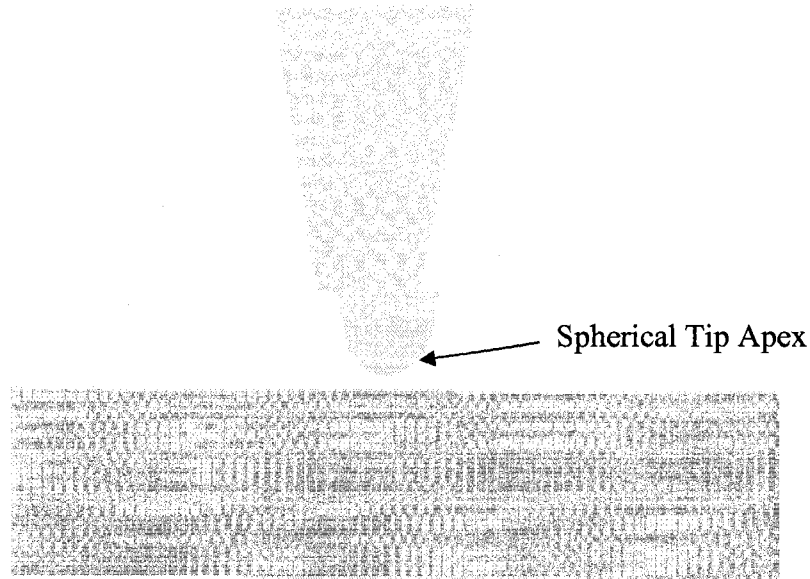
(b)



(c)



(d)



(e)

Figure 12. Geometry of AFM probe 2. (a) Front view of whole of the AFM probe-substrate system, (b) Side view of the AFM probe, (c) Orthogonal view of the AFM probe, (d) Side view of the pyramidal tip cone and the part of cantilever, (e) Spherical tip apex at the end of the tip.

5.2 Meshing of Atomic Force Microscope Probes

Meshing is a very critical part of finite element analysis to obtain accurate finite element analysis simulation results. One critical requirement for proper meshing is that both the conductors associated with the electrostatic analysis must have reasonably identical mesh conformity. The AFM probe-substrate system is a very complex structure to mesh due to geometric properties of AFM probe and the inclination of the AFM probe cantilever with respect to substrate. Different parts of AFM probes have different dimensions ranging from a few hundred micrometers associated with the cantilever geometry to some nanometers associated with the radius of curvature of the tip. As to carry out electrostatic

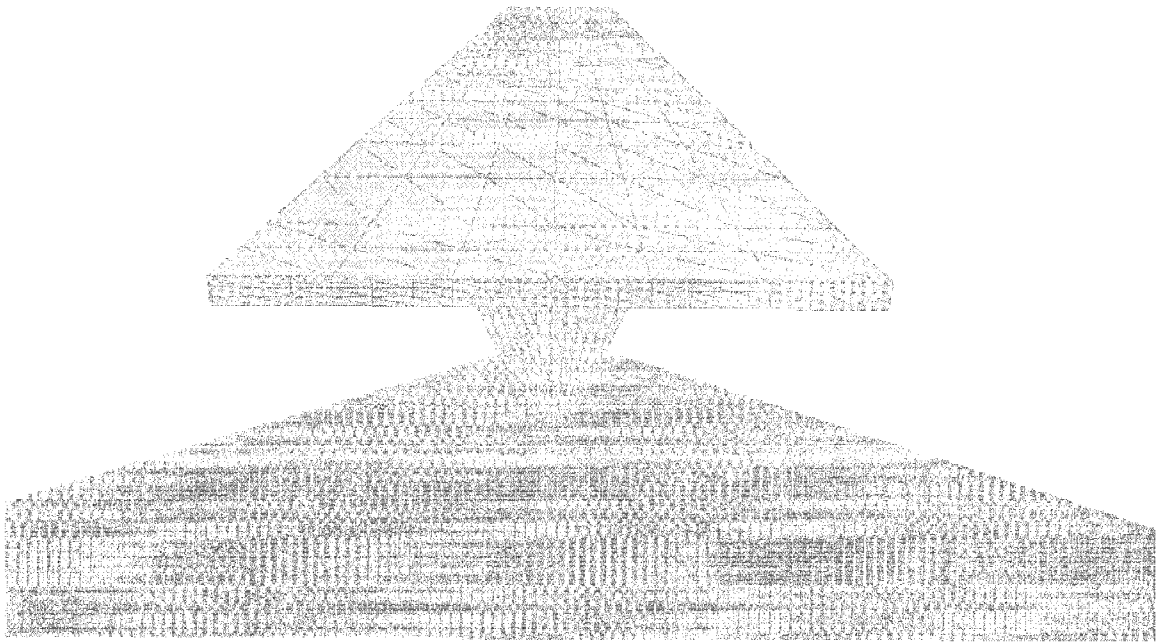
analysis, both the conductors must have reasonably identical meshing to compute the electrostatic force accurately, the substrate region under the spherical cone tip must have reasonably identical mesh structure as the spherical cone tip. However, as the spherical cone tip has a radius of less than 200 nm for the probes under consideration, refining the substrate mesh to that scale makes the problem size extremely large to be solved using even high performance machines with 4 GB of memory. On the other hand, the substrate region under the cantilever has almost similar dimensions.

For these reasons, using the local mesh refinement feature of IntelliSuite, different part of the structure are meshed in such a way that maintains a reasonably identical mesh structure between the exposed faces where electric flux lines are supposed to terminate. To realize these meshes, each probe has been divided into three separate geometries containing the cantilever, the pyramidal tip cone and the spherical tip apex. Despite this, due to the nm scale dimensions of the spherical cone apex, it was difficult to achieve reasonable mesh conformity in the region between the spherical tip apex and the substrate. To overcome this, a novel feature of IntelliSuite, called *Elec_mesh* has been used to activate the Exposed Face Mesh algorithm (EFM). When compared to the commonly used volume refining mesh method, the EFM algorithm shows substantial improvement in increasing accuracy of results and reducing computational time and memory expenses. It is to be noted here that in order to calculate the electrostatic pressure on these Exposed Faces, the commonly used method is to refine the three-dimensional domain. Unfortunately, the modeling of typical electrostatically activated MEMS devices using the volume mesh method results in large problem sizes. Instead of refining the volume mesh, *Elec_mesh* can be used to refine only the electrostatic surface mesh on chosen Exposed Faces. The advantage of this novel method is that the electrostatic surface mesh is separated from the mechanical volume mesh while assuring full compatibility between the two. The EFM method results in smaller computational models while improving the numerical accuracy in MEMS simulation. Actual refinement process depends on the refinement factor. Selecting a refinement factor of 4 actually refines the mesh $2 \times N^2$ or 32 times. Also, additional simplification can be made to the electrostatic surface mesh. For example, inputting a refinement factor of 0 for selected faces will

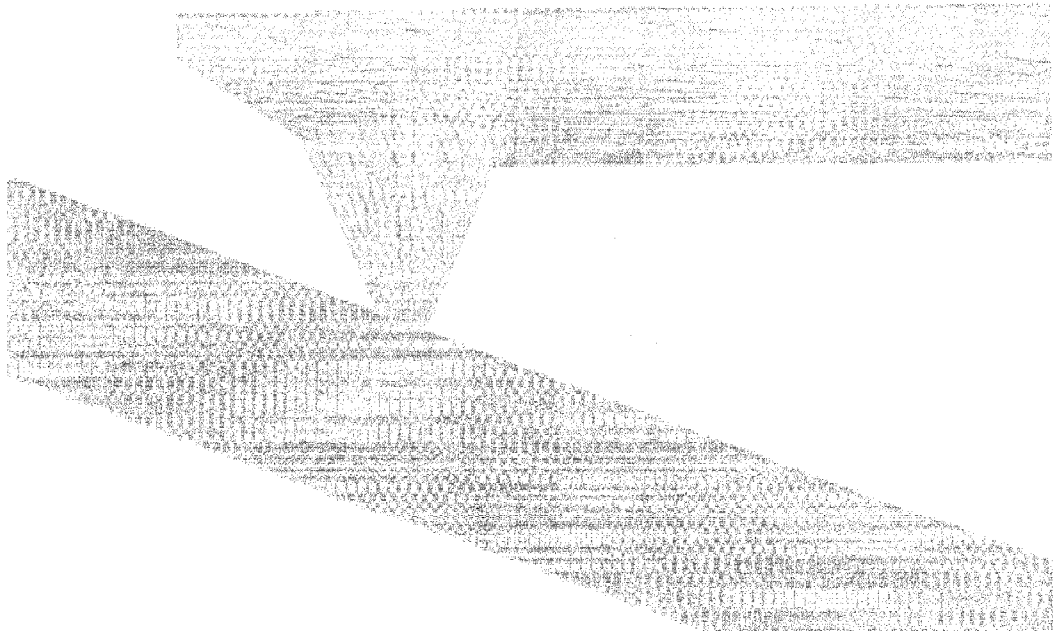
allow that face to have no mesh, thus removing it from the electrostatic analysis. As the bottom surface of the substrate isn't contributing to any electrostatic force for the probe deflection, removing the electrical mesh from that surface will reduce the problem size. Similarly, the fixed face of the probe (rigid support end) also isn't contributing to the electrostatic force for the probe deflection. Thus removing the electrical mesh from that face also reduces the problem size. To model the electrostatic force more accurately, the substrate region near the probe tip has been refined sharply using this electrical mesh feature to achieve reasonable mesh conformity between the spherical cone tip and the substrate. A refinement factor $N=6$ for the tip cone and the spherical tip apex and $N=4$ for the substrate region near the probe tip have been used for the electrical mesh.

5.2.1 Meshing of the Probes

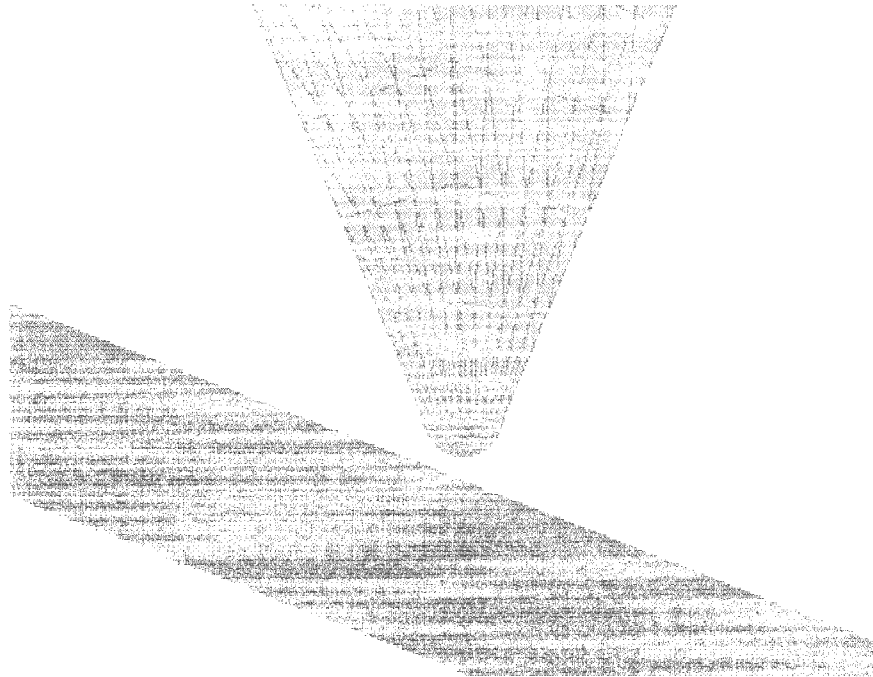
Both the probes are meshed following the strategy described in the previous section. Figure 13 shows the meshed geometry of the AFM probe 1 and figure 14 shows the meshed geometry of the AFM probe 2. Both the figures highlight the local mesh refinement at different parts of the structures. In the figures, the triangular panels represent the electrical mesh that is superimposed on the original quadrilateral mechanical mesh.



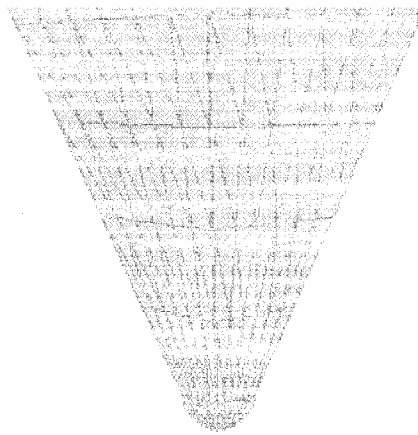
(a)



(b)

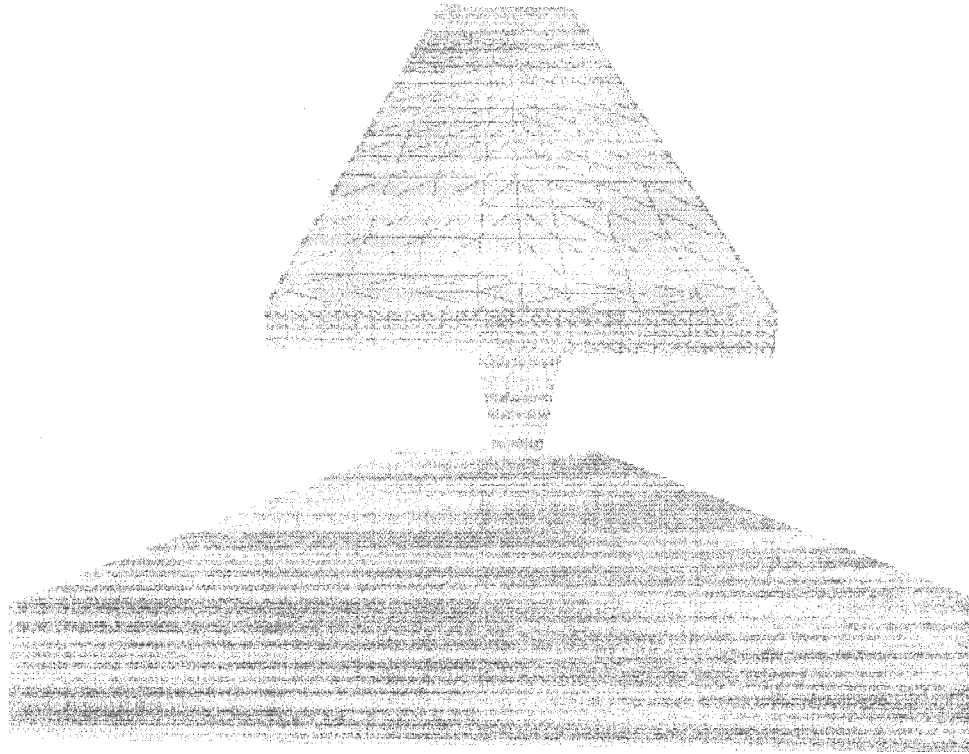


(c)

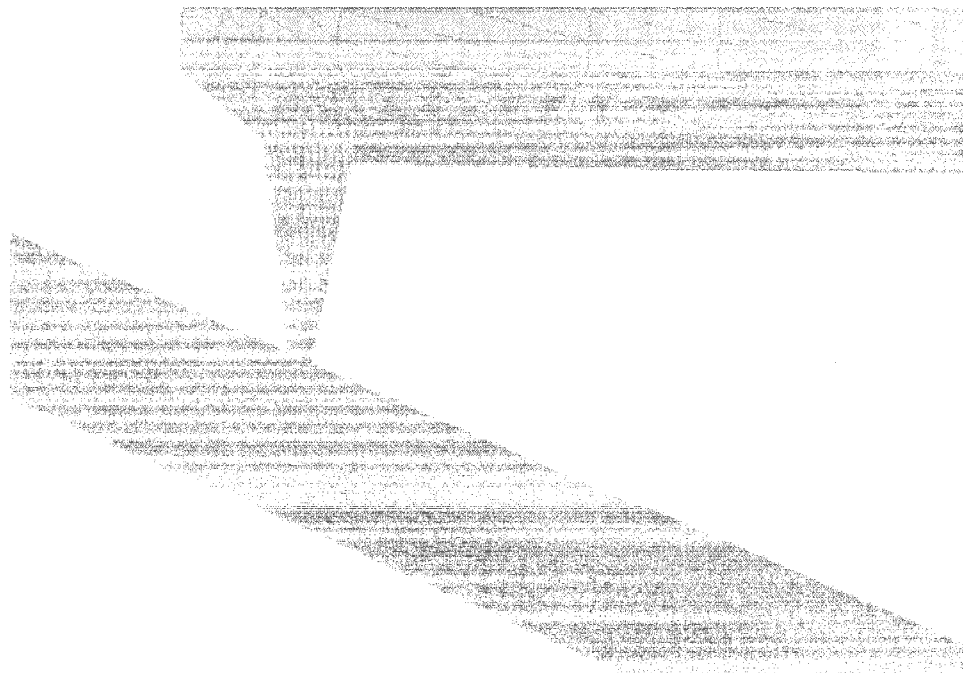


(d)

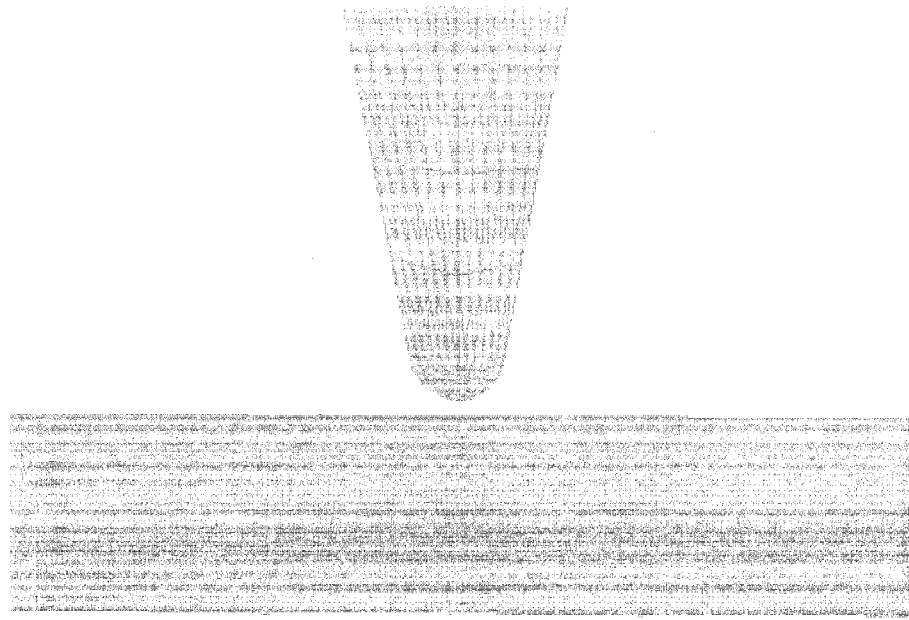
Figure 13. Different mesh sizes for different part of AFM probe 1. (a) Front view of the meshing of the AFM probe and the substrate, (b) Side view of the meshing of the pyramidal tip cone and the substrate, (c) Front view of the meshing of the tip apex, (d) Side view of the meshing of tip apex.



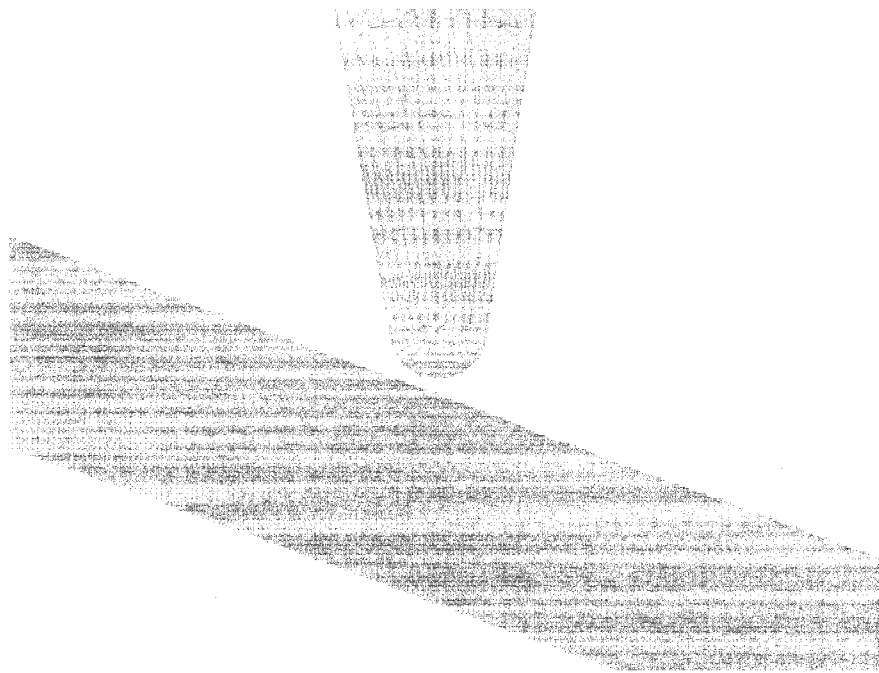
(a)



(b)



(c)



(d)

Figure 14. Different mesh sizes for different part of AFM probe 2. (a) Front view of the meshing of the AFM probe and the substrate, (b) Side view of the meshing of the pyramidal tip cone and the substrate, (c) Front view of the meshing of the tip apex, (d) Side view of the meshing of tip apex.

Chapter Summary

In this Chapter detailed construction and meshing strategy of 3-D solid models of two AFM probe having different geometric specifications using the IntelliSuite™ 3-D builder™ has been presented. Difficulties associated with the meshing of the structures have been discussed. To achieve reasonably conformal meshing between the cantilever, cone, spherical cone apex, and the substrate, local mesh refinement has been used. Further refinement was carried out using the IntelliSuite's novel Elec_mesh feature that allows refining the electrical mesh only to a very high factor and then superimposing the refined electrical mesh in the form of triangular panels on the original quadrilateral mechanical mesh. This reduces problem size considerably, improves accuracy and minimizes analysis time and memory expenses. The meshed geometry is then used to carry out 3-D electromechanical finite element analysis as described in the next chapter.

CHAPTER 6

MODEL VERIFICATION

This chapter describes the verification method of the developed closed-form analytical model to determine the pull-in voltage of an AFM probe. To verify the model's accuracy, the model predicted results for the pull-in voltage for different AFM probe geometries with varying initial gaps have been compared with some published experimentally determined values as well as with the results from another published curve model. The new model predicted values have also been compared with the results obtained from the 3-D electromechanical finite element analysis results using IntelliSuite. The developed model is found to be in excellent agreement with the experimental and the curve model published elsewhere as well as with FEA results. This 3-way cross-verification clearly establishes the very high degree of accuracy of the newly developed pull-in voltage model as well as the model for the stored electrostatic energy.

6.1 Comparison with Experimentally Determined Values and Values Determined from a Published Model

The authors in [12] have done experiments to determine the pull-in voltage of an AFM probe for different initial gaps between the spherical tip apex and the substrate. Geometrical specifications of the AFM probe used in the experiment are identical with the probe 1 specifications as listed in Table 1 and the material properties of the probe are listed in Table 2. The experimentally determined pull-in voltage values are listed in Table 3 along with the values predicted by the new model, the curve model in [12], and the

results from IntelliSuite™ 3-D electromechanical FEA. In each case, % deviations from the experimentally determined values are also provided.

Table 2. AFM probe Material properties (AFM probe 1)

Young Modulus, E (GPa)	165
Poison's ratio, ν	0.23
Residual stress, σ	0

Table 3. Pull-in Voltage Comparison for Different Methods (AFM probe 1)

Initial gap, \hat{w}_0 (nm)	V_{PI} (volts) Experimental Ref [12]	V_{PI} (volts) Published model [12]	V_{PI} (volts) New Model	V_{PI} (volts) FEA	$\Delta\%$ Exp [12]- FEA	$\Delta\%$ Exp.[12]- Ref. [12]	$\Delta\%$ Exp. - New model
150	13.5	13.25	13.67	14	3.70	1.85	1.26
175	15	14.83	15.33	15.6	4	1.13	2.2

From Table 3, it is clear that the new model predicted pull-in voltage values are in excellent agreement with published experimentally determined values with a maximum percent deviation of only 2.2%. Result comparisons for experimental, model in [12] and the new model for some other different initial distances are shown in Table 4.

Table 4. Pull-in Voltage comparison (AFM probe 1)

Initial gap, \hat{w}_0 (nm)	V_{PI} (volts) Experimental [12]	V_{PI} (volts) Published model [12]	V_{PI} (volts) New Model	$\Delta\%$ Exp – Published model [12]	$\Delta\%$ Exp – New model
100	10.30	9.92	10.02	3.69	2.72
125	11.9	11.69	11.97	1.76	0.59
200	16.35	16.25	16.9	0.61	3.36

From Table 4, it is clear that for a range of 100–200 nm initial distances, the new model predicted values have the lowest maximum deviation from experimental values of 3.36 % where as the curve model in [12] deviates from the experimental values by a maximum of 3.69 %. This clearly establishes the superiority of the new model in terms of accuracy compared to the curve model in [12].

Figure 15 shows a graphical comparison between the pull-in voltage values predicted by the new model and the model in [12] for different initial distances for the probe specifications listed in Table 2. From the figure, it is evident that both the models are in excellent agreement with experimental results over a wide range of initial distances.

The parameters which are needed for the curve model in [12] to predict the pull-in voltage have been extracted from the experimental results when the initial distance between tip apex and substrate is 217 nm. For this reason the curve model in [12] predicts the pull-in voltage more accurately around 200 nm initial distances. And as the electrostatic terms in energy expression have been expanded by Taylor series around the zero deflection position while developing the new model, so when the initial distance between AFM tip apex and substrate increases, it introduces error slightly to the new model.

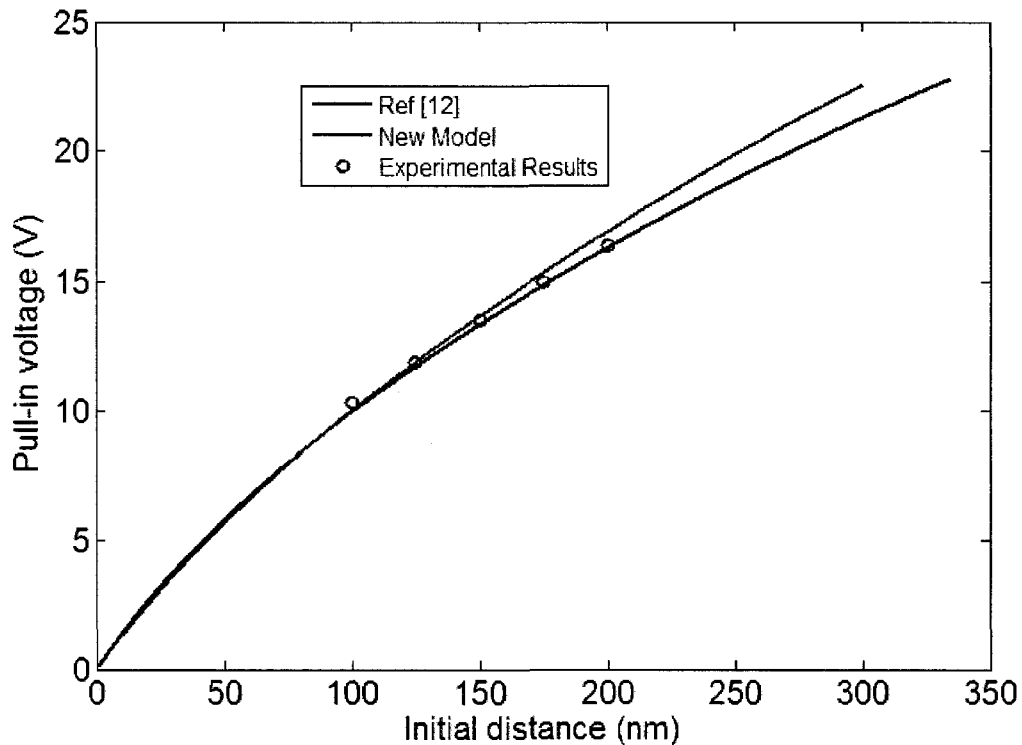


Figure 15. Pull-in voltage comparison of new closed-form model and published curve model in [12] with experimental results [12]

A graphical comparison of the pull-in voltage values predicted by the model in [12] with experimental values [12] is shown in figure 16 that shows that the curve model is in excellent agreement with experimental results. As the new model is also in excellent agreement with the curve model as it is evident from figure 15, this again clearly establishes that the new model maintains its accuracy consistently over a wide range of initial distances. However, unlike the curve model, the new model doesn't need any prior experimentally determined values to establish some operating parameter values in their model as discussed in chapter 1. Thus the new model is easier and can readily be used for predicting the pull-in voltage values for any initial distance without any expensive experimental measurements.

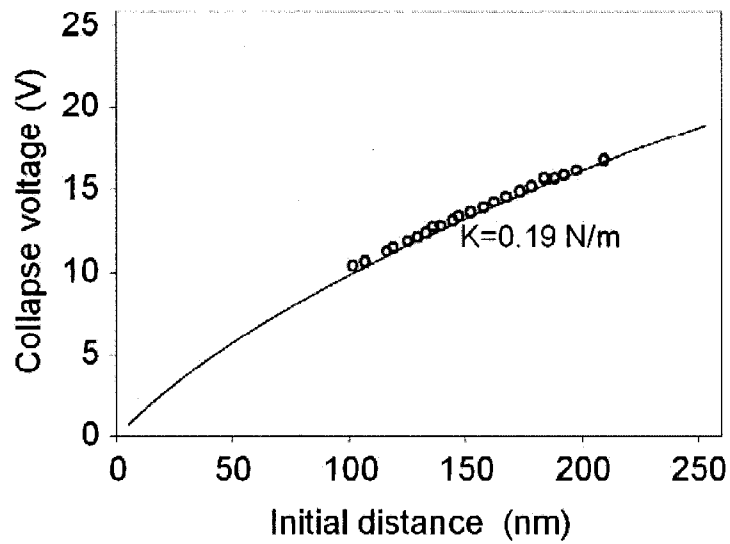


Figure 16. Initial distance vs. Pull-in voltage curve from [12]

6.2 Comparison with Finite Element Analysis (FEA) Results

Thermoelectromechanical (TEM[®]) module of IntelliSuite[™] has been used to simulate both the AFM probes with specifications listed in Table 1. Simulations for both of these probes have been carried out for different initial gaps between the spherical tip apex and the substrate. Figures 17 and 18 show the state of spherical tip apexes for probe 1 and probe 2, respectively, after the collapse of the probe on to the substrate due to pull-in. The displacement of different parts of AFM probe 1 and probe 2 after they collapsed onto the substrate are shown in figures 19 and 20, respectively.

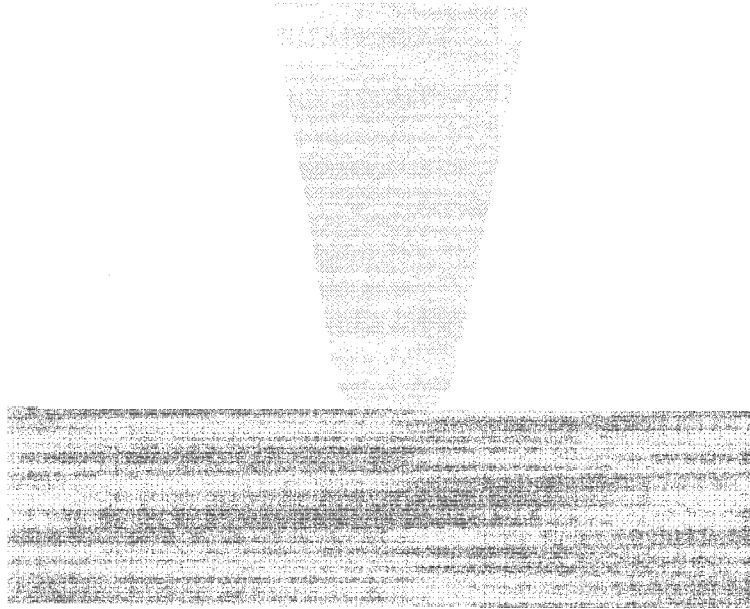


(a)

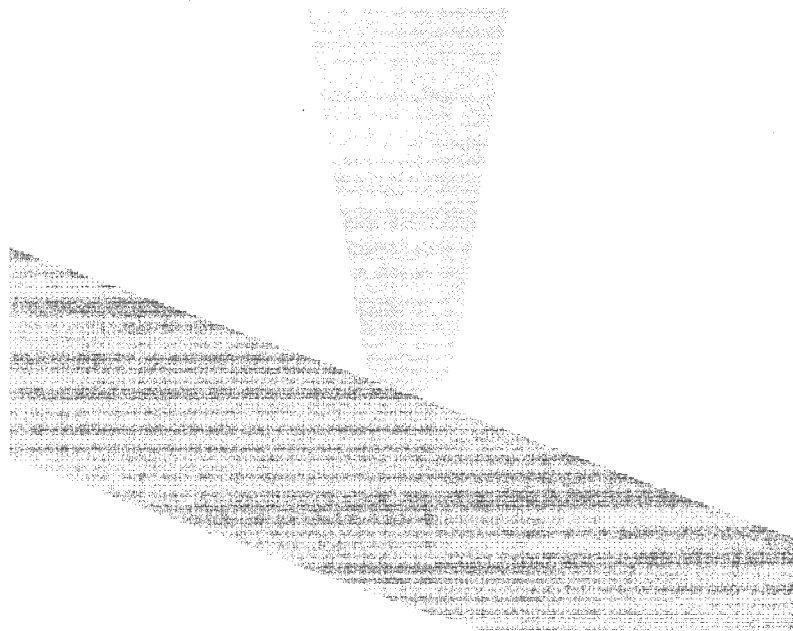


(b)

Figure 17. Pull-in of the spherical tip apex of AFM probe 1 onto the substrate. (a) Front view (b) Side view.



(a)



(b)

Figure 18. Pull-in of the spherical tip apex of AFM probe 2 onto the substrate. (a) Front view (b) Side view.

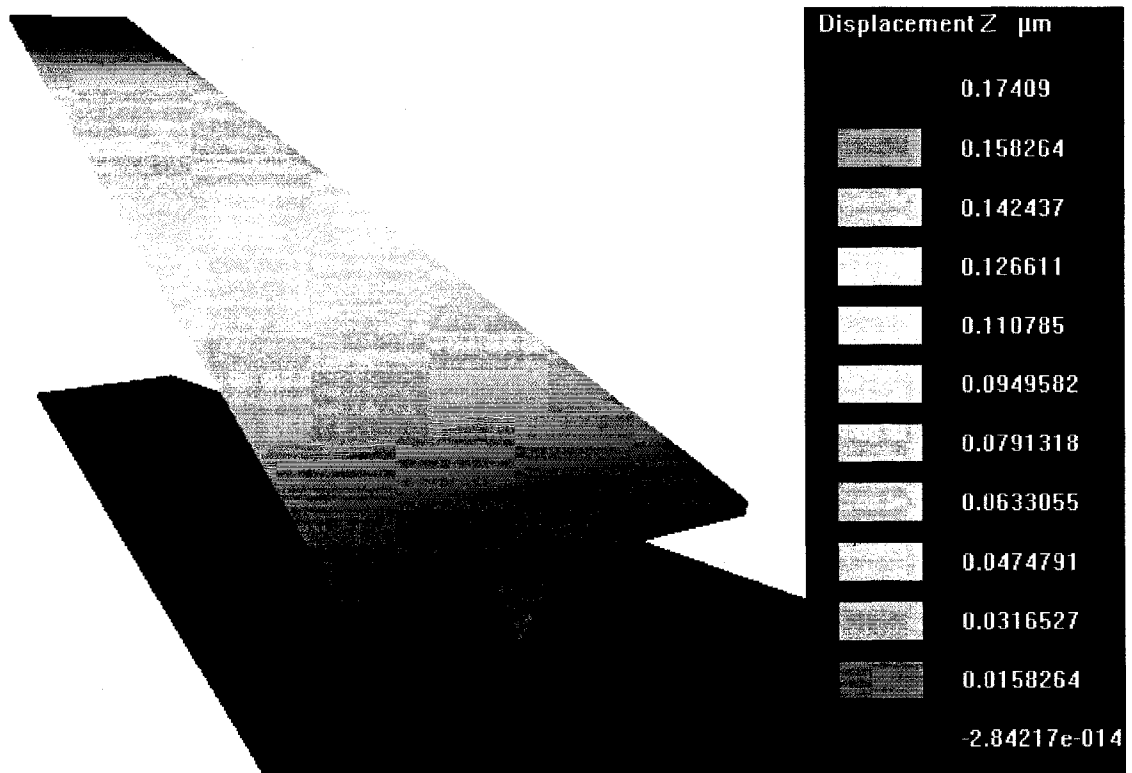


Figure 19. Visualization of the displacement of different parts of AFM probe 1 in a color scale.

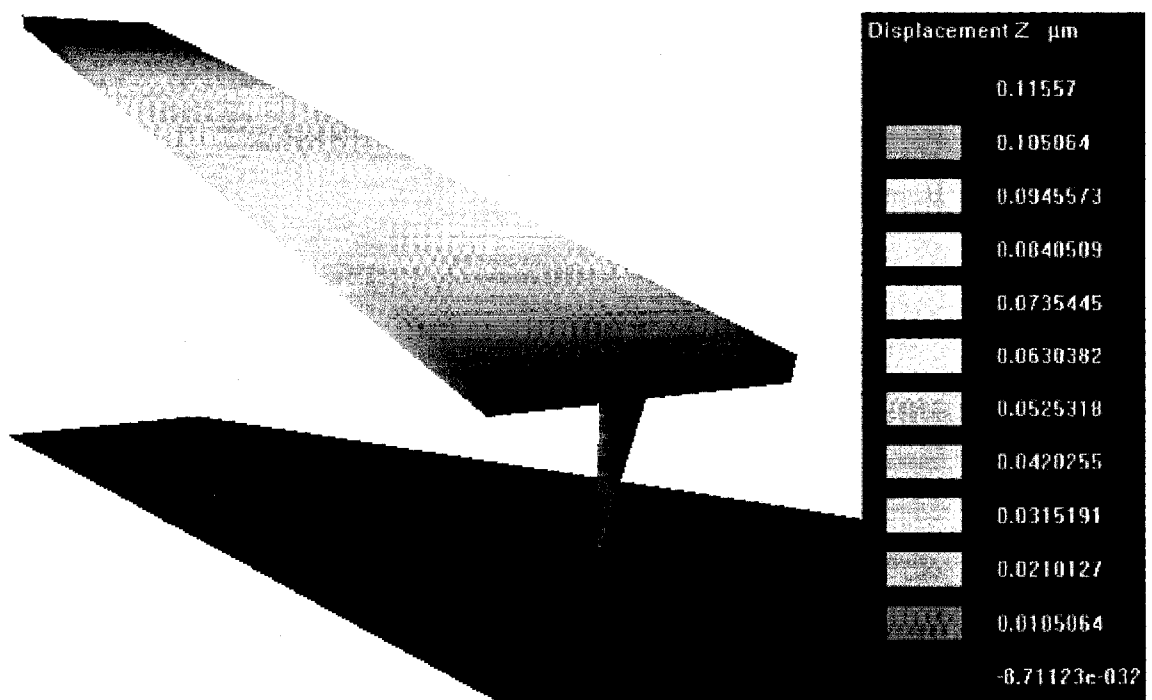


Figure 20. Visualization of the displacement of different parts of AFM probe 2 in a color scale.

FEA results for different initial gaps between the spherical tip apex and the substrate and also for different material properties for both the probe geometries are shown in Tables 5 and 6, respectively.

Table 5. Pull-in Voltage from FEA (AFM probe 1)

Initial gap, \hat{w}_0 (nm)	Young modulus, E (GPa)	Poisson's ratio, ν	V_{PI} (volts) IntelliSuite FEA
174	165	0.23	15.6
150	165	0.23	14.0
157	140	0.06	13.1

Table 6. Pull-in Voltage from FEA (AFM probe 2)

Initial gap, \hat{w}_0 (nm)	Young modulus, E (GPa)	Poisson's ratio, ν	V_{PI} (volts) IntelliSuite FEA
115	165	0.23	37.4
139	165	0.23	41.7
150	140	0.06	42.1
155	165	0.23	47.2

Comparisons between the FEA results and the new model predicted values are shown in Tables 7 and 8, respectively.

Table 7. Pull-in Voltage Comparison with FEA and New Model (AFM probe 1)

Initial gap, \hat{w}_0 (nm)	Young modulus, E (GPa)	Poisson's ratio, ν	V_{PI} (volts) IntelliSuite FEA	V_{PI} (volts) Closed-form Model	$\Delta\%$ FEA results – New model
174	165	0.23	15.6	15.27	2.11
150	165	0.23	14.0	13.67	2.35
157	140	0.06	13.1	12.7	3.05

Table 8. Pull-in Voltage Comparison with FEA and New Model (AFM probe 2)

Initial gap, \hat{w}_0 (nm)	Young modulus, E (GPa)	Poisson's ratio, ν	V_{PI} (volts) IntelliSuite FEA	V_{PI} (volts) Closed-form Model	$\Delta\%$ FEA results – New model
115	165	0.23	37.4	33.85	9.49
139	165	0.23	41.7	38.27	8.22
150	140	0.06	42.1	38.07	9.57
155	165	0.23	47.2	43.57	7.69

It is evident from Tables 7 and 8 that for both the probes the new model is in good agreement with IntelliSuite FEA results. For probe 1, the new model is in excellent agreement with the FEA results having a maximum deviation of only 3.05 %. For probe 2, the new model predicted values deviate from IntelliSuite FEA results by 9.57%.

This apparent large deviation of new model predicted pull-in voltages for Probe 2 from IntelliSuite FEA results can be attributed to the mesh size mismatch between the spherical tip apex of AFM probe and the substrate. Minimum mesh size in the spherical tip apex is around 200 square nm whereas the minimum mesh size in the substrate just beneath the spherical tip apex is 6250 square nm. Ratio of the minimum mesh size in the substrate underneath and the spherical tip apex is 31.25. This mesh size mismatch underestimates the electrostatic fields between the spherical tip apex and the substrate underneath. This underestimated electrostatic field results in a lower electrostatic force that consequently results in a higher pull-in voltage value. Another point is, as the half opening angle θ of the probe 1 tip cone is almost 2.5 times greater than that of the probe 2, the surface area associated with the probe 1 tip cone is larger than that of probe 2 tip cone. Consequently, the effect of mesh size mismatch at the end of the tip cone is less dominant for probe 1 compared to probe 2. This explains higher accuracy of the FEA results for probe 1 compared to probe 2.

Explanations provided by IntelliSuite Support through personal communication also support this explanation. Figures 13 and 14 show the complexity of meshing the structures. It is to be noted here that with the mentioned mesh size, the FEA problem had 10,200 mechanical nodes which were further refined using the electrical mesh with a factor of 72 ($N=6$) for the tip cone and the tip apex. It took 8 days to complete the simulation in a Pentium quad processor machine with 4 GB of physical memory.

Chapter summary

In this chapter the newly developed closed-form analytical model to determine the pull-in voltage of an AFM probe has been verified by comparing the model predicted values with experimentally determined values, values predicted by a model published elsewhere, and 3D electromechanical FEA results for different initial gaps between the tip cone and the substrate for two different AFM probes. Excellent agreement between the results establishes high degree of accuracy of the newly developed model. Additionally, the new model is easier and can readily be used for predicting the pull-in voltage values for any initial distance without any expensive experimental measurements as is necessary in a curve model published elsewhere[12].

CONCLUSION

In this thesis, the development and verification of a highly accurate closed-form analytical model to determine the pull-in voltage of an Atomic Force Microscope probe under electrostatic actuation has been presented. The newly developed closed-form model is readily computable without the need for any experimentally extracted parameters as necessary in an existing curve model published elsewhere [12]. This closed-form analytical model considers the fringing field capacitances between the inclined rectangular cross-section cantilever of the AFM probe and the surface (substrate) under it to more accurately predict the stored electrostatic energy in the AFM probe system.

Inclusion of the fringing field capacitance helped to develop a more accurate expression for the stored electrostatic energy. The developed closed-form analytical model takes account of the nonlinear nature of the electromechanical coupling of the AFM probe. Energy method has been adopted to obtain the analytical solution of the pull-in voltage. The closed-form analytical model has been derived based on the Euler-Bernoulli theory, Taylor series expansion of the total electrostatic energy, deflection function of the first natural mode of cantilever beam and Cardan solutions.

At First the total energy including the van der Waals energy, electrostatic energy and mechanical bending energy, of the AFM probe-substrate system has been derived. Due to the very short range effect of van der Waals energy, it has been neglected in the determination of pull-in voltage model. The mechanical bending energy has been derived on assumptions of Euler-Bernoulli beam.

Nonlinear terms in the electrostatic energy expression have been linearized using a Taylor series expansion method and higher order terms in the expansion series have been truncated to realize a more compact expression of the linearized electrostatic energy. First natural mode of the beam has been assumed as the deflection shape function of the beam. An expression for the weighting parameter associated with the first natural mode of vibration at pull-in has been derived. This expression is then substituted in the second derivative of the total energy expression. At pull-in, the second derivative of the stored energy goes to zero. This condition is then utilized to solve the second derivative of the energy expression to yield the target closed-form model for the pull-in voltage.

After the development of the closed-form model, the verification of the new closed-form model has been presented. To verify the model's accuracy, the model predicted values for the pull-in voltage for different AFM probe geometries with varying initial gaps have been compared with some published experimentally determined values as well as with the results from another published curve model. The new model predicted values have also been compared with the results obtained from 3-D electromechanical finite element analysis results using IntelliSuite. The developed model is found to be in excellent agreement with minimum deviation of 0.59% and maximum deviation of 3.36 % from the experimental results. It has also been determined that the model maintains its accuracy consistently over a wide range of initial gap between the spherical tip apex and the substrate underneath when compared with experimental and curve model predicted values. The new model is also in very much agreement with the finite element analysis results using IntelliSuite™ having a maximum deviation of 9.57 % for one probe and 3.05% for another probe. Investigation shows that this apparent large deviation of pull-in voltage for former probe predicted by new model and finite element analysis results is due to minimum mesh size mismatch between the spherical tip apex and the substrate underneath and is a limitation of IntelliSuite software.

Thus, the goal of developing a highly accurate readily computable straight forward closed-form analytical model for determining the pull-in voltage of an AFM probe under electrostatic load has been achieved in this thesis work. And as there is no necessary for

any experimentally extracted parameters, the new model offers the opportunity to observe the influence of the physical parameters of an AFM probe on pull-in voltage and load-deflection characteristic.

Future Direction

Experiments can be performed with different AFM probes using different Atomic Force microscope to further verify the accuracy of the developed model and to find out the range of accuracy of this model. Short range van der Waals energy can also be incorporated so that the model becomes effective even in the range of van der Waals attractive forces. Experiments can be done to find out the accuracy of the incorporation of van der Waals forces. Once the experimental values for the pull-in voltage have been gathered for different sets of AFM probes in a wide range of probe substrate distance, besides the first natural mode of the cantilever beam, different deflection shape functions such as uniform load deflection shape function and point load shape function can also be investigated in the range of van der Waals forces or out of the range of van der Waals forces.

REFERENCES

- [1] G. Binnig, C. F. Quate, and C. Gerber, "Atomic Force Microscope," *Phys. Rev. Lett.*, vol. 56, pp. 930-933, Mar. 1986.
- [2] J. M. R. Weaver and D.W. Abraham, "High resolution atomic force microscopy potentiometry," *J. Vac. Sci. Technol. B*, vol. 9, pp. 1559-1561, May 1991.
- [3] J. E. Stern, B. D. Terris, and H. J. Mamin, "Deposition and imaging of localized charge on insulator surfaces using a force microscope," *Appl. Phys. Lett.*, vol. 53, pp. 2717-2719, Dec. 1988.
- [4] B. D. Terris, J. E. Stern, D. Rugar, and H. J. Mamin, "Contact electrification using force microscopy," *Phys. Rev. Lett.*, vol. 63, pp. 2669-2672, Dec. 1989.
- [5] J. Hu, X. D. Xiao, and M. Salmeron, *Appl. Phys. Lett.* "Scanning Polarization force microscopy: A technique for imaging liquids and weakly absorbed layers," *Phys. Lett.*, vol. 67, pp. 476-478, Jul. 1994.
- [6] Y. Martin and H. K. Wickramasinghe, "Magnetic imaging by "force microscopy" with 1000 Å resolution," *Appl. Phys. Lett.*, vol. 50, pp. 1455-1457, May. 1987.
- [7] S. Jegadesan, R. C. Advincola, and S. Valiyaveetil, "Nanolithographic Electropolymerization of a Precursor Polymer Film to Form Conducting Nanopatterns," *Adv. Mater. (Weinheim, Ger.)*, vol. 17, pp. 1282-1285, Mar. 2005.
- [8] D. Wouters, R. Willems, and S. Hoepfener, "Oxidation Conditions for Octadecyl Trichlorosilane Monolayers on Silicon: A Detailed Atomic Force Microscopy Study of the Effects of Pulse Height and Duration on the Oxidation of the Monolayer and the Underlying Si Substrate," *Adv. Funct. Mater.*, vol. 15, pp. 938-944, May. 2005.
- [9] S. Decossas, F. Mazen, T. Baron, G. Brémond and A. Souifi, "Atomic force microscopy nanomanipulation of silicon nanocrystals for nanodevice fabrication," *Nanotechnology*, vol. 14 pp. 1272-1278, Oct. 2003.
- [10] H. W. Lee, S. H. Kim, Y. K. Kwak, E. S. Lee and C. S. Han, "The effect of the shape of a tip's apex on the fabrication of an AFM tip with an attached single carbon nanotube," *Sensor Actuators A*, vol. 125, pp. 41-49, Oct. 2005.

- [11] J. E. Kim and C. S. Han, "Use of dielectrophoresis in the fabrication of an atomic force microscope tip with a carbon nanotube: a numerical analysis," *Nanotechnology*, vol. 16, pp. 2245-2250, Aug. 2005.
- [12] J Toset, I Casuso, J Samitier and G Gomila, "Deflection–voltage curve modeling in atomic force microscopy and its use in DC electrostatic manipulation of gold nanoparticles," *Nanotechnology*, vol. 18, 015503 (9pp).
- [13] S. Chowdhury, M. Ahmadi, and W. C. Miller, "A Closed-Form Model for the Pull-in Voltage of Electrostatically Actuated Cantilever Beams," *J. Micromech. Microeng.*, vol. 15, pp. 756-763, Feb. 2005.
- [14] Y. C. Hu, "Closed Form Solutions for the Pull-in Voltage of Micro Curled Beams Subjected to Electrostatic Loads," *J. Micromech. Microeng.*, vol. 16, pp. 648-655, Feb. 2006.
- [15] S. Gomez-Monivas, L. S. Froufe-Perez A. J. Caamano, "Electrostatic Forces between Sharp Tips and Metallic and Dielectric Samples," *Appl. Phys. Lett.*, Vol 79, pp. 4048-50, Dec. 2001.
- [16] G. M. Sacha, J. J. Saenz, "Cantilever effects on electrostatic force gradient microscopy," *Appl. Phys. Lett.*, Vol 85, pp. 2610-2, Sep. 2004.
- [17] M. Saint Jean, S. Hudlet, C. Guthmann, and J. Berger "Van der Waals and Capacitive Forces in Atomic Force Microscopies," *J. Appl. Phys.*, vol. 86, pp. 5245-5248, Nov. 1999.
- [18] S. Belaidi, P. Girard, and G. Leveque, "Electrostatic forces acting on the tip in atomic force microscopy: Modelization and comparison with analytic expressions," *J. Appl. Phys.*, vol. 81, pp. 1023-1030, Feb. 1997.
- [19] E. Bonaccorso, F. Schönfeld, and H. J. Butt, "Electrostatic forces acting on tip and cantilever in atomic force microscopy," *Phys. Rev. B*, vol. 74, 085413, Aug. 2006.
- [20] J. Colchero, A. Gil, and A. M. Baro, "Resolution enhancement and improved data interpretation in electrostatic force microscopy," *Phys. Rev. B*, Vol. 64, 245403 (11pp), Nov. 2001.
- [21] B. M. Law and F. Rieutord, "Electrostatic forces in atomic force microscopy," *Phys. Rev. B*, vol. 66, 035402 (6pp), Jul. 2002.

- [22] J. M. Rabaey, *Digital Integrated Circuits*. Englewood Cliffs, NJ: Prentice Hall, 1996, pp 438-445.
- [23] W. H. Chang, "Analytic IC-Metal-Line Capacitance Formulas," *IEEE Trans. Microw. Theory Tech.*, vol. MTT-24, pp. 608–611, Sep. 1976.
- [24] E. Barke, "Line-to-Ground capacitance calculation for VLSI: A comparison," *IEEE Trans. Comput.-Aided Design Integr. Circuits Syst.*, vol. 7, no. 2, pp. 295–298, Feb. 1988.
- [25] W. T. Weeks, "Calculation of Coefficients of Capacitance for Multiconductor Transmission Lines in the Presence of a Dielectric Interface," *IEEE Trans. Microw. Theory Tech.*, vol. MTT-18, no. 1, pp. 35–43, Jan. 1970.
- [26] N. P. Van Der Meijs and J. T. Fokkema, "VLSI Circuit Reconstruction From Mask Topology," *Integration*, vol. 2, no. 2, pp. 85–119, Mar. 1984.
- [27] M. I. Elmasry, "Capacitance Calculation in MOSFET VLSI," *IEEE Electron Device Letters*, Vol. EDL-3, No. 1, pp. 6-7, Jan. 1982.
- [28] T. Sakurai and K. Tamaru, "Simple Formulas for two and Three Dimensional Capacitances," *IEEE Transactions on Electron Devices*, Vol. ED-30, No. 2, pp. 183-185, Feb. 1983.
- [29] C. P. Yuan and T. N. Trick, "Calculation of Capacitance in VLSI Circuits," in *Proc. of IEEE Conference on Computer-Aided Design*, 1984, pp. 263-265.
- [30] S. Hudlet, M. Saint Jean, and C. Guthmann, "Evaluation of the capacitive force between an atomic force microscopy tip and a metallic surface," *Eur. Phys. J. B*, vol. 2, pp. 5-10, Apr. 1998.
- [31] J. A. Turner, S. Hirsekorn, U. Rabe, W. Arnold, "High-frequency response of atomic force microscope cantilevers," *J. Appl. Phys.*, vol. 82, pp. 966-979, Aug. 1997.
- [32] D. Sarid, *Scanning Force Microscopy*, New York, NY: Oxford University Press, 1994, pp. 9-12.
- [33] W. Soedel, *Vibration of Shells and plates*, 2nd Edition, New York, NY: Dekker, 1993, pp.71.

- [34] R. Legtenberg, J. Gilbert, S. D. Senturia and M. Elwenspoek “Electrostatic Curved Electrode Actuators,” *J. Microelectromech. Syst*, vol. 6, pp. 257-265, Sep. 1997.
- [35] M. R. Spiegel, *Mathematical Handbook of Formulas and Tables*, New York, NY: McGraw-hill, 1887, pp. 32.

APPENDIX A

MATLAB SCRIPTS

This appendix presents the matlab scripts necessary for the simulation of the developed closed-form model to determine pull-in voltage developed. The matlab scripts which are necessary for the simulation are Vinfring4th.m, A1fringfunc.m, A2fringfunc.m, A3fringfunc.m, A4fringfunc.m, F1Lenght4th.m, F1Width4th.m, F1Thickness4th.m, F2Lenght4th.m, F2Width4th.m, F2Thickness4th.m, F3Lenght4th.m, F3Width4th.m, F3Thickness4th.m, F4Lenght4th.m, F4Width4th.m, F4Thickness4th.m, F5fring4th.m, phixfring4th.m, phixppfring4th.m, itafring4th.m. The top most matlab scripts is Vinfring4th.m. The rest of the matlab scripts are presented in a sequence by which they are called from the top script Vinfring4th.m. The script z0vsVinfring4thplot.m has been used to generate initial distances vs. pull-voltage curve.

Vinfring4th.m Script

```
function Vin=Vinfring4th(z0in)

global L z0 vlever h Wd T R theta a b c d A1 A2 A3 A4
z0=z0in;                               %%%%% Initial distance between apex and substrate

E0=8.854187816*10^-12;                   %%%%% Permittivity of free space
L=450*10^-6;                             %%%%% Length of the AFM probe Cantilever
Wd=50*10^-6;                             %%%%% Width of the AFM probe Cantilever
T=2*10^-6;                               %%%%% Thickness of the AFM probe Cantilever
```

```

h=17*10^-6;          % Height of Tip Cone
R=118*10^-9;        % Radius of the spherical tip Apex
vlever=21*pi/180;   % inclination angle of the Cantilever
theta=23*pi/180;    % half opening angle of Tip Cone

a=2*pi*R;
b=R*(1-sin(theta));
c=R*cos(theta)^2/sin(theta);
q=1/(log(tan(theta/2)))^2;
d=pi*q;

E_young=165*10^9;   % Young's modulus of cantilever material
v=0.23;             % Poison ratio of cantilever material
Y_mod_E=E_young/(1-v^2); % Effective Young's modulus
I=Wd*T^3/12;        % cross sectional area moment of inertia

A1=A1fringfunc();
A2=A2fringfunc();
A3=A3fringfunc();
A4=A4fringfunc();

F5=quadl(@F5fring4th,0,L,1e-18);

ita=itafring4th();
num=2*(Y_mod_E*I*F5);
den=E0*(2*A2+6*ita*A3+12*A4*ita^2);
Vin=sqrt(num/den);

```

A1fringfunc.m Script

```
function A1=A1fringfunc()
```

```
global L z0 vlever h Wd T R theta a b c d
```

```
phixL=phixfring4th(L);
```

```
GL=gfunctionfring4th(L);
```

```
A11length=Wd*quadr(@F1Lenght4th,0,L,1e-18);
```

```
A11Width=0.265*(Wd^0.25)*quadr(@F1Width4th,0,L,1e-18);
```

```
A11Thickness=0.53*(T^0.5)*quadr(@F1Thickness4th,0,L,1e-18);
```

```
A11=A11length+A11Width+A11Thickness;
```

```
A1Tip=0.53*Wd*(T^0.5)/GL^1.5;
```

```
A12=( -log( (z0+b)/h ) - 1);
```

```
A13=( c/(z0+b) );
```

```
A14=( b/(z0*(z0+b)) );
```

```
A1=A11 + ( A1Tip + 2*d*( A12 + A13 ) + a*A14 )*phixL;
```

A2fringfunc.m Script

```
function A2=A2fringfunc()
```

```
global L z0 vlever h Wd T R theta a b c d
```

```
phixL=phixfring4th(L);
```

```
GL=gfunctionfring4th(L);
```

```

A21length=Wd*quadr(@F2Lenght4th,0,L,1e-18);
A21Width=(5.3/32)*(Wd^0.25)*quadr(@F2Width4th,0,L,1e-18);
A21Thickness=(3.18/8)*(T^0.5)*quadr(@F2Thickness4th,0,L,1e-18);
A21=A21lenght+A21Width+A21Thickness;

```

```

A2Tip=(3.18/8)*Wd*(T^0.5)/GL^2.5;

```

```

A22=1/( 2*(z0+b) );
A23=c/( 2*(z0+b)^2 );
A24=(2*z0^2*b + b^2)/( 2*z0^2*(z0+b)^2 );
A2=A21 + ( A2Tip + 2*d*( A22 + A23 ) + a*A24 )*phixL^2;

```

A3fringfunc.m Script

```

function A3=A3fringfunc()

```

```

global L z0 vlever h Wd T R theta a b c d

```

```

phixL=phixfring4th(L);
GL=gfunctionfring4th(L);

```

```

A31length=Wd*quadr(@F3Lenght4th,0,L,1e-18);
A31Width=(15.9/128)*(Wd^0.25)*quadr(@F3Width4th,0,L,1e-18);
A31Thickness=(5.3/16)*(T^0.5)*quadr(@F3Thickness4th,0,L,1e-18);
A31=A31lenght+A31Width+A31Thickness;

```

```

A3Tip=(5.3/16)*Wd*(T^0.5)/GL^3.5;

```

```

A32=1/( 6*(z0+b)^2 );

```

```

A33=c/( 3*(z0+b)^3 );
A34=(3*z0^2*b+3*z0*b^2+b^3)/(3*z0^3*(z0+b)^3);
A3=A31 + ( A3Tip + 2*d*( A32 + A33 ) + a*A34 )*phixL^3;

```

A4fringfunc.m Script

```

function A4=A4fringfunc()

global L z0 vlever h Wd T R theta a b c d

phixL=phixfring4th(L);
GL=gfunctionfring4th(L);

A41length=Wd*quadl(@F4Lenght4th,0,L,1e-18);
A41Width=(206.7/2048)*(Wd^0.25)*quadl(@F4Width4th,0,L,1e-18);
A41Thickness=(37.1/128)*(T^0.5)*quadl(@F4Thickness4th,0,L,1e-18);
A41=A41length+A41Width+A41Thickness;

A4Tip=(37.1/128)*Wd*(T^0.5)/GL^4.5;

A42=1/( 12*(z0+b)^3 );
A43=c/( 4*(z0+b)^4 );
A44=(4*z0^3*b+6*z0^2*b^2+4*z0*b^3+b^4)/(4*z0^4*(z0+b)^4);
A4=A41 + ( A4Tip + 2*d*( A42 + A43 ) + a*A44 )*phixL^4;

```

F1Lenght4th.m Script

```
function F1 = F1Lenght4th(x)
    G = gfunctionfring4th(x);
    phix = phixfring4th(x);
    F1=(phix./(G.^2));
```

F1Width4th.m Script

```
function F1Width = F1Width4th(x)
    G = gfunctionfring4th(x);
    phix = phixfring4th(x);
    F1Width=(phix./(G.^1.25));
```

F1Thickness4th.m Script

```
function F1Thickness = F1Thickness4th(x)
    G = gfunctionfring4th(x);
    phix = phixfring4th(x);
    F1Thickness=(phix./(G.^1.5));
```

F2Lenght4th.m Script

```
function F2=F2Lenght4th(x)
    G = gfunctionfring4th(x);
    phix= phixfring4th(x);
    F2 = ((phix.^2)./(G.^3));
```

F2Width4th.m Script

```
function F2Width = F2Width4th(x)
    G = gfunctionfring4th(x);
    phix = phixfring4th(x);
    F2Width=((phix.^2)./(G.^2.25));
```

F2Thickness4th.m Script

```
function F2Thickness = F2Thickness4th(x)
    G = gfunctionfring4th(x);
    phix = phixfring4th(x);
    F2Thickness=((phix.^2)./(G.^2.5));
```

F3Lenght4th.m Script

```
function F3=F3Lenght4th(x)
    G = gfunctionfring4th(x);
    phix= phixfring4th(x);
    F3 = ((phix.^3)./(G.^4));
```

F3Width4th.m Script

```
function F3Width = F3Width4th(x)
    G = gfunctionfring4th(x);
    phix = phixfring4th(x);
    F3Width=((phix.^3)./(G.^3.25));
```

F3Thickness4th.m Script

```
function F3Thickness = F3Thickness4th(x)
    G = gfunctionfring4th(x);
    phix = phixfring4th(x);
    F3Thickness=((phix.^3)/(G.^3.5));
```

F4Lenght4th.m Script

```
function F4=F4Lenght4th(x)
    G = gfunctionfring4th(x);
    phix= phixfring4th(x);
    F4 = ((phix.^4)/(G.^5));
```

F4Width4th.m Script

```
function F4Width = F4Width4th(x)
    G = gfunctionfring4th(x);
    phix = phixfring4th(x);
    F4Width=((phix.^4)/(G.^4.25));
```

F4Thickness4th.m Script

```
function F4Thickness = F4Thickness4th(x)
    G = gfunctionfring4th(x);
    phix = phixfring4th(x);
    F4Thickness=((phix.^4)/(G.^4.5));
```

F5fring4th.m Script

```
function F5=F5fring4th(x)
phixpp= phixppfring4th(x);
F5 = (phixpp.^2);
```

phixfring4th.m Script

```
function phix= phixfring4th(x)
global L
lamda=1.875/L;
sigma=(sinh(lamda*L)-sin(lamda*L))/(cosh(lamda*L)+cos(lamda*L));
phix=((cosh(lamda.*x)-cos(lamda.*x))-sigma.*(sinh(lamda.*x)-sin(lamda.*x)));
```

phixppfring4th.m Script

```
function phixpp = phixppfring4th(x)
global L
lamda=1.875/L;
sigma=(sinh(lamda*L)-sin(lamda*L))/(cosh(lamda*L)+cos(lamda*L));
phixpp=cosh(lamda*x)*lamda^2+cos(lamda*x)*lamda^2-
sigma*(sinh(lamda*x)*lamda^2+sin(lamda*x)*lamda^2);
```

phixppfring4th.m Script

```
function G = gfunctionfring4th(x)
global L z0 vlever h
```

```
G=z0+h*cos(vlever)+L*sin(vlever)-x*sin(vlever);
```

itafring4th.m Script

```
function ita=itafring4th()
global L z0 vlever h Wd T R theta A1 A2 A3 A4

M=(A1/A4)/16 - (A3/A4)^3/512;
N=-(A3/A4)^2/64;
S=( M + sqrt(N^3+M^2) )^(1/3);
T=( M - sqrt(N^3+M^2) )^(1/3);
ita=S+T-A3/(8*A4);
```

z0vsVinfring4thplot.m Script

```
function z0vsVinfring4thplot()
k=30;
Vin=zeros(1,k);
for i=1:k
    z0in=10e-9*i;
    Vin(i)=Vinfring4th(z0in);
end
z02=10:10:300;
plot(z02,Vin,':m'); hold on;
```

APPENDIX B

DEFINITION OF USED SYMBOLS

A	hamakar constant of the AFM tip apex
C_T	total capacitance between the AFM probe and the substrate
C_{lever}	capacitances between the AFM probe cantilever and the substrate
C_{cone}	capacitances between the AFM tip cone and the substrate
C_{apex}	capacitances between the AFM tip apex and the substrate
E	young's modulus
E_e	energy associated with electrostatic force
E_m	energy associated with mechanical restoring force
E_T	total energy of the AFM probe-substrate system
E_{vdw}	energy associated with van der Waals force
\tilde{E}	effective young's modulus
F_e	electrostatic force
F_m	mechanical restoring force
F_{vdw}	van der Waals forces
$g(x)$	variable gap between the AFM probe cantilever and the substrate
G	initial gap between the AFM probe cantilever and the substrate
H	height of the AFM tip cone
I	cross sectional area moment of inertia
k_1	flexural wave number of the first natural mode
L	length of the AFM probe cantilever
P	weighting of the first natural mode

P_n	weighting of the associated nth mode of deflection shape function
P_{PI}	value of P at Pull-in
P_1	weighting of the first natural mode
R	radius of the AFM probe tip apex
t	thickness of the AFM probe cantilever
ν	Poisson's ratio
V	applied bias voltage
V_{PI}	pull-in voltage
w	width of the AFM probe cantilever
\hat{w}	beam deflection as a function of axial position x ,
\hat{w}_0	initial distance between the AFM tip apex and the substrate
x	axial position along the length of AFM probe cantilever
z	instantaneous distance between the AFM tip apex and the substrate
z_c	pull-in distance between the AFM tip apex and the substrate
z_0	initial distance between the AFM tip apex and the substrate
β_{lever}	inclination angle of the AFM probe with respect to substrate plane
ϵ_r	relative permittivity of dielectric spacer
ϵ_0	permittivity of free space
$\varphi(x)$	first natural mode of clamped free beam
$\varphi_n(x)$	nth assumed deflection shape function of clamped free beam
$\varphi_1(x)$	first natural mode of clamped free beam
θ	half opening angle of the AFM tip cone

VITA AUCTORIS

Liton Ghosh was born in 1981 in Dhaka, Bangladesh. He obtained his Bachelor of Applied Science in Electrical and Electronics Engineering from Bangladesh University of Engineering and Technology (BUET) in Dhaka, Bangladesh, where he graduated in 2005. He is currently a candidate for the degree of Master of Applied Science in Electrical and Computer Engineering in the fields of Microelectromechanical Systems (MEMS) at the University of Windsor, Windsor, Canada.